The spherical design algorithm in the numerical simulation of biological tissues with statistical fibre-reinforcement

(Article begins on next page)

Noname manuscript No.
(will be inserted by the editor)

The Spherical Design Algorithm in the numerical simulation of biological tissues with statistical fibre-reinforcement

Melania Carfagna · Alfio Grillo

Received: date / Accepted: date

DOI: 10.1007/s00791-017-0278-6
Available online: April 21, 2017
Journal: *Computing and Visualization in Science* (2017) 18: 157–184 (Springer)

Abstract Nowadays, the description of complex physical systems, such as biological tissues, calls for highly detailed and accurate mathematical models. These, in turn, necessitate increasingly elaborate numerical methods as well as dedicated algorithms capable of resolving each detail which they account for. Especially when commercial software is used, the performance of the algorithms coded by the user must be tested and carefully assessed. In Computational Biomechanics, the Spherical Design Algorithm (SDA) is a widely used algorithm to model biological tissues that, like articular cartilage, are described as composites reinforced by statistically oriented collagen fibres. The purpose of the present work is to analyse the performances of the SDA, which we implement in a commercial software for several sets of integration points (referred to as "spherical designs"), and compare the results with those determined by using an appropriate set of points proposed in this manuscript. As terms for comparison we take the results obtained by employing the integration scheme `Integral`, available in Matlab®. For the numerical simulations, we study a well-documented benchmark test on articular cartilage, known as 'unconfined compression test'. The reported numerical results highlight the influence of the fibres on the elasticity and permeability of this tissue. Moreover, some technical issues of the SDA (such as the choice of the quadrature points and their position in the integration domain) are proposed and discussed.

Keywords Spherical Design Algorithm · Quadrature Methods · Fibre-reinforced Materials · Finite Element Method

This work has been partially financed by the *Politecnico di Torino* and the *Fondazione Cassa di Risparmio di Torino* in the context of the funding campaign "*La Ricerca dei Talenti*" (HR Excellence in Research)

M. Carfagna · A. Grillo
Dept of Mathematical Sciences (DISMA) "G.L. Lagrange", Politecnico di Torino, C.so Duca degli Abruzzi 24, 10129, Torino (TO) Italy
Tel.: +39-011-0907531
Fax: +39-011-0907599
E-mail: melania.carfagna@polito.it

E-mail: alfio.grillo@polito.it

1 Introduction

Soft biological tissues are often described as complex porous media filled with an interstitial fluid. The complexity of these media, formed by the co-existence of several structural units with different physical and chemical properties, is related to their internal structure and composition, which render them highly heterogeneous and anisotropic materials. Several multiphasic models of biological tissues have been developed (cf. e.g. [3, 13,23,26,39,41,45]), in which the Theory of Mixtures is employed to account for the fact that the interstitial fluid comprises several constituents (like, for example, ionic species, nutrients for the cells and byproducts of cellular metabolic reactions), and that different types of solid materials (e.g. biological proteins, extra-cellular matrix, and collagen fibres) characterise the overall properties of the "solid phase" of a tissue. Among the solid constituents of biological tissues, collagen fibres provide a reinforcing function and their distribution and orientation make the tissues anisotropic.

For example, this is the case of tendons, arterial walls [24,37,49], articular cartilage [17,41,46], and heart [52].

It is believed that a different arrangement of the fibre network, which may result to be either structurally organised or not, corresponds to a different functionality of the tissue [5,60]. In fact, this is particularly the case of articular cartilage (a sheath of soft connective tissue covering the opposing ends of bone in diarthrodial joints [46]), in which the collagen fibres are concentrated throughout the tissue in a nonuniform way and are oriented statistically according to some point-dependent probability density distribution [19,58]. More precisely, histological experiments performed on articular cartilage show that three (sometimes four [46]) zones can be distinguished in the tissue, roughly layered along the direction of the tissue's depth and determined by the characteristic alignment of the collagen fibres in addition to other properties of the tissue. In the so-called "deep zone", which is close to the interface, also referred to as "tidemark", that separates the cartilage from the subchondral bone, the fibres are principally oriented perpendicularly to the tidemark; in the "middle zone" the fibres are oriented almost randomly; finally, in the "upper zone" the fibres tend to be parallel to the articular surface, i.e., the surface on which the sheaths of cartilage covering the opposing bones of the diarthrodial joint exchange loads reciprocally. The pattern of fibre orientation depicted above influences the stiffness of the tissue as well as its capability of conveying the interstitial fluid throughout its pores. In many cases of interest, a fair approximation of the material behaviour of articular cartilage can be achieved by regarding the tissue as transversely isotropic [17,58], which means that its material properties are invariant under rotations about a given symmetry axis. Moreover, the solid phase of articular cartilage is often assumed to be hyperelastic with respect to some undeformed configuration, and its principal solid and fluid constituents are regarded as intrinsically incompressible. The latter hypothesis implies that the overall tissue's compressibility is related to the evolution of its porosity, which accompanies the flow of the interstitial fluid when the tissue is compressed. Hereafter, the dynamics of the interstitial fluid is assumed to be governed by Darcy's law. Recently, however, possible deviations from Darcy's regime have been investigated in [28], on the basis of the theory reported in [10]. In the sequel, the hyperelastic, inhomogeneous, and transversely isotropic material model of articular cartilage studied in [58] will be adopted. This model considers a statistical distribution of collagen fibres and, thus, introduces directional averaging operators to determine the overall tissue's properties from those associated with one family of fibres aligned along a given direction of space. More specifically, if the distribution of orientations is assumed to be continuous, the averaging operators are integrals defined over the set of all possible spatial directions. In the context of this work, such integrals will be used to obtain the overall strain energy density and the overall permeability of the considered tissue sample. The fibre orientation pattern is described by a point-dependent probability density distribution, which serves as a weight for the averaging integrals, thereby modulating the influence of each family of fibres.

The description of the mechanical response of articular cartilage, which includes the study of the flow of the interstitial fluid, is often referred to as the "biphasic model of cartilage" [46]. Within a purely mechanical framework, and in its standard formulation, the biphasic model consists of two coupled equations, which represent the mass and momentum balance laws for the tissue as a whole. The model equations are obtained by means of closure conditions that relate the tissue's porosity with the volumetric deformation, and the fluid filtration velocity with the pressure gradient inside the tissue. The first relation is a consequence of incompressibility, which for porous media does not necessarily restrict the deformation to be isochoric, whereas the second relation stems from Darcy's law and, thus, introduces the tissue's permeability tensor.

When the biphasic model of articular cartilage accounts for the inhomogeneity and anisotropy of the tissue, and the statistical orientation of the collagen fibres is considered in the constitutive relations of the stress and permeability, the model equations become highly nonlinear and coupled with one another. In such situations, Finite Element (FE) methods are usually adopted to search for numerical solutions. Still, besides the techniques elaborated for solving the model equations numerically, either problem-dependent approximation criteria [34] or dedicated quadrature methods must be developed for computing the integrals that determine the directional averages of the constitutive functions defining the mechanical stress and tissue's permeability. In general, indeed, these quantities depend on the orientation of the fibres and on the deformation in a non-separable way [34], so that it is not possible to compute *exactly* the averaging integrals *before* starting the FE method. A rather largely employed algorithm, referred to as Spherical Design Algorithm (SDA), is usually coupled with the FE method to solve the averaging integrals at each time step and linearisation iteration of the solution procedure. The SDA treats the averaging integrals determining the stress and the permeability of articular cartilage as integrals defined over the surface of a unit sphere centred at each point of the region of space occupied by the tissue. The implementation of the SDA is explained in detail and its reliability is tested against a different quadrature scheme, which is available in Matlab.

It must be recalled that the issue of spherical integration is "quite old" (see e.g. [6,44]), and it has been recently used for fibre-reinforced biological tissues (see, e.g., [18,57]). Our work aims to contribute, in the framework of the constitutive modelling of tissues, to the long-standing problem of the integration over the surface of the sphere. This is done with the purpose of determining the constitutive information supplied by the statistical orientation of the reinforcing collagen fibres. However, in other contexts, several authors have proposed both analytical and numerical arguments for providing accurate and efficient numerical integration schemes [6,44,14,57]. Among those, a general method for obtaining conceptually integration formulae was demonstrated by Bažant and Oh [6]. Nevertheless, to our understanding, what in other circumstances makes a numerical scheme better than others finds only practical and fortuitous evidences. In [6], it is remarked that the integration points should be chosen in a way to maintain their symmetric and regular distribution on the surface of the sphere. For instance, a particularly entangling choice of the set of points can be obtained by means of a projection of vertices, and, more generally, of points lying on the edges of polyhedra inscribed in the sphere [6]. Some collections of Spherical t-Designs generated with the aid of this projection method are reported also in [38]. In [57], the weights and quadrature points obtained by Lebedev [44] have been selected as the best choice for performing *angular integrations*, among other quadrature methods. Thus, unluckily, as also pointed out in [57], the best set of quadrature points for the SDA is extremely problem-dependent, possibly related to the symmetries of the function to be integrated, and, in general, the *degree of the formula*, i.e., the degree of the polynomials that can be resolved exactly, is not a sufficient condition to ensure the accuracy of the numerical integration for a less smooth and regular function. In particular, two different Spherical t-Designs with the same accuracy could lead to extremely different numerical performances when applied to a particular benchmark. As we show in the following, the SDA accuracy strongly depends not only on the number of points (representing the directions of the fibres) by which we approximate the integration, but also on the particular way in which they are arranged on the domain of integration, whereas the Matlab algorithm that has been used for comparison only depends on the user-defined degree of approximation, and adaptively chooses nodes and points for the quadrature.

The paper is organised as follows: The biphasic model of articular cartilage, as formulated in [58], is summarised in Section 2. The probability density distributions and the constitutive laws specifically adopted for articular cartilage are reported in Section 3. The structure of the considered quadrature schemes, and in particular of the SDA, is presented in Section 4. The integration procedures are tested in Section 5, in which a well-established benchmark problem is analysed. The results of the benchmark test are commented in Section 6. Finally, some concluding remarks and plans for future work are outlined in Section 7.

2 Biphasic Model of Articular Cartilage

The non-linear, poroelastic biphasic model of articular cartilage (AC) has been investigated in several publications with different level of complexity, depending on whether the anisotropy and inhomogeneity of the tissue are accounted for (cf., e.g. [28,29,31,58]). Since a detailed presentation of the model has been recently given in [58] (although the presence of ions and their influence on the tissue mechanics were neglected), we recall here for the sake of completeness the main hypotheses and logical steps leading to the equations that have to be ultimately solved. Consistently with the approach followed in other articles, and for the sake of generality, we employ the covariant formalism of Continuum Mechanics [47], along with the modifications put forward in [19]. The theoretical apparatus, on which the biphasic model of AC is developed, rests on two pillars: (i) Hybrid Mixture Theory [9,35], and (ii) Poroelasticity.

2.1 Microstructure

In this section, we summarise the description of the microstructure of AC, as presented in [58]. Within the approximation presented in the following, the ionic phase of AC is not accounted for (cf. e.g. [45,46] for a review on the role of electric charges on the mechanics of AC). At a sufficiently coarse level of description, the main constituents of AC are represented by a matrix of proteoglycans, chondrocytes (i.e., cells secreting the extracellular matrix), collagen fibres, and an interstitial fluid capable of flowing throughout the tissue [46]. It is assumed that the fluid saturates completely the tissue and, since the focus of the present study is not on the chondrocytes, it is also hypothesised that matrix and chondrocytes can be regarded as a single entity. Moreover, in the sense explained in [58], the existence of a Representative Elementary Volume (REV) is claimed, in which all considered tissue's constituents coexist. The portion of REV occupied by the fluid is described by the volumetric fraction ϕ_{f}. Due to the assumption of saturation, the volumetric fraction of the solid constituents is defined by $\phi_{\mathrm{s}} := 1 - \phi_{\mathrm{f}}$. As in [58], ϕ_{s} is given by the sum $\phi_{\mathrm{s}} = \phi_{0\mathrm{s}} + \phi_{1\mathrm{s}}$, where $\phi_{0\mathrm{s}}$ and $\phi_{1\mathrm{s}}$ denote, respectively, the volumetric fractions of matrix and fibres, expressed per unit solid volume of the REV. Since the tissue is inhomogeneous and deforms, the volumetric fractions are generally function of space and time. From here one, the complex "matrix-and-fibres" existing at each point of the tissue will be referred to as "the solid phase" of AC. Analogously, the fluid can also be referred to as the "fluid phase" of AC.

2.2 Kinematics

Within the framework of Mixture Theory, the kinematics of AC can be formulated as in [54,55], and subsequently adapted in [58] to fibre-reinforced porous media. The major hypothesis is that the solid phase of AC can be associated with a *reference configuration* $\mathscr{B}$. The motion of the solid phase is described by the one-parameter family of smooth mappings

$$\chi(\,\cdot\,,t) : \mathscr{B} \to \mathbb{R}^3, \tag{1}$$

which map the point $X \in \mathscr{B}$ into $x = \chi(X,t) \in \mathbb{R}^3$, at each time $t \in \mathscr{I}$ of the time interval $\mathscr{I}$.

To define the motion of the fluid, the 3D material manifold $\mathscr{M}_{\mathrm{f}}$ is introduced, whose elements, i.e., the fluid particles $\mathscr{X}_{\mathrm{f}} \in \mathscr{M}_{\mathrm{f}}$, are embedded into $\mathbb{R}^3$ by means of the one-parameter family of mappings

$$\mathfrak{f}(\,\cdot\,,t) : \mathscr{M}_{\mathrm{f}} \to \mathbb{R}^3. \tag{2}$$

The subset of $\mathbb{R}^3$ defined by

$$\mathscr{B}_t := \chi(\mathscr{B},t) \cap \mathfrak{f}(\mathscr{M}_{\mathrm{f}},t) \tag{3}$$

is the region of space occupied at time $t \in \mathscr{I}$ by the tissue, viewed as a solid-fluid mixture. In (3), $\chi(\mathscr{B},t)$ and $\mathfrak{f}(\mathscr{M}_{\mathrm{f}},t)$ are the images of $\chi(\,\cdot\,,t)$ and $\mathfrak{f}(\,\cdot\,,t)$ at $t \in \mathscr{I}$, respectively. The volumetric fractions $\phi_{\mathrm{f}}(\,\cdot\,,t)$, $\phi_{0\mathrm{s}}(\,\cdot\,,t)$, and $\phi_{1\mathrm{s}}(\,\cdot\,,t)$ are defined as scalar fields over $\mathscr{B}_t$. Moreover, at each $x \in \mathscr{B}_t$, the vectors $\boldsymbol{v}_{\mathrm{s}}(x,t) = \dot{\chi}(X,t)$ and $\boldsymbol{v}_{\mathrm{f}}(x,t) = \dot{\mathfrak{f}}(\mathscr{X}_{\mathrm{f}},t)$ denote the velocities of the solid phase and of the fluid particle $\mathscr{X}_{\mathrm{f}}$ passing through x at time t. The superimposed dot means partial differentiation with respect to time. The two-point, second-order tensor $\boldsymbol{F}(X,t)$, definable through the directional derivative of χ at $(X,t) \in \mathscr{B} \times \mathscr{I}$, i.e.,

$$(\partial_{\boldsymbol{U}}\chi)(X,t) = \boldsymbol{F}(X,t)\boldsymbol{U}, \tag{4}$$

with $\boldsymbol{U}$ being a vector attached at X, is commonly referred to as the deformation gradient of the solid phase [47]. With respect to an appropriate tensor basis, its components read $F^a{}_A = \partial\chi^a/\partial X^A$, with $a, A = 1,2,3$. It is important to remark that, as in [58], also in this work matrix and fibres share the same velocity, $\boldsymbol{v}_{\mathrm{s}}(x,t)$, at all times and at all points. To complete the kinematic picture, the volumetric ratio $J = \det(\boldsymbol{F}) > 0$, and the right Cauchy-Green deformation tensor $\boldsymbol{C} = \boldsymbol{F}^{\mathrm{T}}\boldsymbol{g}\boldsymbol{F}$ are introduced. Here, $\boldsymbol{g}$ denotes the metric tensor associated with $\mathbb{R}^3$. For future use, we also introduce the metric tensor associated with the undeformed configuration, $\boldsymbol{G}$.

In the sequel, we adopt a rather standard notation in Continuum Mechanics (cf., e.g., [47]). Let f be a function of space and time expressing a given physical quantity. Without loss of generality, we may assume that $f(x,t)$, with $x \in \mathbb{R}^3$ and $t \in \mathscr{I}$, is a scalar, but it could generally represent a vector or a tensor of any order. A function f of this type is sometimes said to provide the "Eulerian description" of the physical quantity with which it is associated. Since for each $X \in \mathscr{B}$ and $t \in \mathscr{I}$ there exists $x \in \mathscr{B}_t \subset \mathbb{R}^3$ such that $x = \chi(X,t)$, the composition $f_{(L)}(\,\cdot\,,t) = f(\,\cdot\,,t) \circ \chi(\,\cdot\,,t) : \mathscr{B} \to \mathbb{R}$ is introduced, which determines the "Lagrangian description" of the considered physical quantity. Hence, it holds that $f_{(L)}(X,t) = f(x,t)$, with $x = \chi(X,t)$. The partial derivative of $f_{(L)}$ with respect to time equals the substantial derivative of f following the solid motion:

$$\begin{aligned}\dot{f}_{(L)}(X,t) &= D_{\mathrm{s}}f(x,t) \\ &= \partial_t f(x,t) + (\operatorname{grad} f(x,t))\boldsymbol{v}_{\mathrm{s}}(x,t),\end{aligned} \tag{5}$$

where $\operatorname{grad} f$ is said to be the *spatial gradient* of f, and $x = \chi(X,t)$. The *material gradient* of $f_{(L)}$, denoted by $\operatorname{Grad} f_{(L)}$, is related to $\operatorname{grad} f$ through

$$\operatorname{grad} f(x,t) = \boldsymbol{F}^{-\mathrm{T}}(X,t)\operatorname{Grad} f_{(L)}(X,t). \tag{6}$$

If $\boldsymbol{q}$ is a spatial vector field, then the divergence of $\boldsymbol{q}$ is given by

$$\begin{aligned}\operatorname{div}\boldsymbol{q}(x,t) &= \boldsymbol{F}^{-\mathrm{T}}(X,t) : \operatorname{Grad}\boldsymbol{q}_{(L)}(X,t) \\ &= \operatorname{tr}\left[\operatorname{Grad}\boldsymbol{q}_{(L)}(X,t)\boldsymbol{F}^{-1}(x,t)\right],\end{aligned} \tag{7}$$

and the symbol ":" stands for "double contraction" between second-order tensors. For the particular case of the solid phase velocity, it holds that

$$\begin{aligned}\operatorname{div}\boldsymbol{v}_{\mathrm{s}}(x,t) &= \boldsymbol{F}^{-\mathrm{T}}(X,t) : \operatorname{Grad}\boldsymbol{v}_{\mathrm{s}(L)}(X,t) \\ &= \dot{J}(X,t)/J(X,t),\end{aligned} \tag{8}$$

where $\boldsymbol{v}_{\mathrm{s}(L)}$ is the Lagrangian counterpart of $\boldsymbol{v}_{\mathrm{s}}$. When $\boldsymbol{q}$ denotes the flux vector associated with a given physical quantity (for example, mass), the material vector

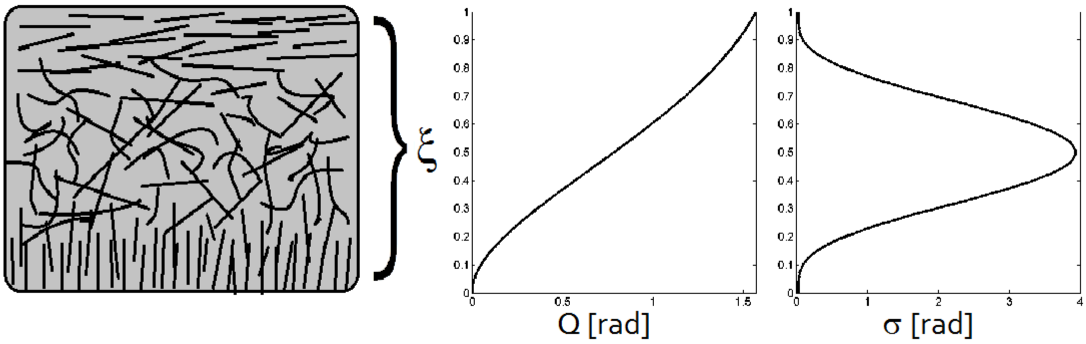

Fig. 1 Graphical representation of a longitudinal section of articular cartilage. The most probable angle of orientation Q, acting as a mean value for the probability density distribution, and the variance have been reported on the right [17]. For both the graphs, the ordinate represents a normalised depth $\xi = X^3/L$.

field $\boldsymbol{Q}$, defined by the equality

$$\boldsymbol{Q}(X,t) = J(X,t)\boldsymbol{F}^{-1}(\chi(X,t),t)\boldsymbol{q}(\chi(X,t),t), \tag{9}$$

is said to be the Piola transformation of $\boldsymbol{q}$ through the motion χ. Hence, recalling Piola's identity $\mathrm{Div}(J\boldsymbol{F}^{-\mathrm{T}}) = \boldsymbol{0}$ [47], we obtain the relation

$$J(X,t)\,\mathrm{div}\,\boldsymbol{q}(\chi(X,t),t) = \mathrm{Div}\,\boldsymbol{Q}\,(X,t) \tag{10}$$

between the spatial divergence of $\boldsymbol{q}$ and the material divergence of $\boldsymbol{Q}$. For example, in a given Cartesian coordinate system, the material divergence $\mathrm{Div}\,\boldsymbol{Q}$ reads

$$\mathrm{Div}\,\boldsymbol{Q} = \frac{\partial Q^A}{\partial X^A} \tag{11}$$

(here, Einstein's convention on repeated indices applies).

2.3 Statistically oriented reinforcing fibres

The tissues addressed in this work are modelled as fibre-reinforced composite materials in which the fibres are oriented statistically. To model the arrangement of the fibres, one introduces the tangent space of $\mathscr{B}$ at X, $T_X\mathscr{B}$, and considers the set

$$\mathbb{S}^2_X\mathscr{B} := \{\boldsymbol{M} \in T_X\mathscr{B} :\ \|\boldsymbol{M}\| = 1\} \tag{12}$$

of all unit vectors (directions) $\boldsymbol{M}$ emanating from X. This set can be taken as representation of the unit sphere centred at X. The probability density distribution of finding a fibre aligned along $\boldsymbol{M} \in \mathbb{S}^2_X\mathscr{B}$ at $X \in \mathscr{B}$ is denoted by $\wp : \mathbb{S}^2_X\mathscr{B} \to \mathbb{R}^+_0$, and must satisfy the normalisation condition $\int_{\mathbb{S}^2_X\mathscr{B}} \wp(\boldsymbol{M}) = 1$. Furthermore, since the phenomena considered in the present context are insensitive to reflections of the unit vectors $\boldsymbol{M}$, $\wp$ must also satisfy the parity condition $\wp(\boldsymbol{M}) = \wp(-\boldsymbol{M})$. We emphasise that $\wp$ is also a function of X. However, in order to keep the notation as light as possible, this dependence will be omitted but understood throughout this work, unless otherwise specified.

Articular cartilage is often modelled as a transversely isotropic material. In particular, in many cases of interest, a global symmetry axis, $\boldsymbol{\xi}$, can be detected, and the material properties of the tissue are invariant under rotations about $\boldsymbol{\xi}$ [58]. Each plane orthogonal to $\boldsymbol{\xi}$ is referred to as *transverse plane*. If the orthonormal vector basis $\{\boldsymbol{\mathcal{E}}_A\}^3_{A=1} \subset T_X\mathscr{B}$ is attached to a given $X \in \mathscr{B}$ in such a way that $\boldsymbol{\mathcal{E}}_3$ is parallel to $\boldsymbol{\xi}$, the unit vector $\boldsymbol{M}$ can be written as

$$\begin{aligned}\boldsymbol{M} &= \hat{\boldsymbol{M}}(\Theta,\Phi)\\ &= \sin\Theta\cos\Phi\,\boldsymbol{\mathcal{E}}_1 + \sin\Theta\sin\Phi\,\boldsymbol{\mathcal{E}}_2 + \cos\Theta\,\boldsymbol{\mathcal{E}}_3,\end{aligned} \tag{13}$$

where the angles $\Theta \in [0,\pi]$ and $\Phi \in [0,2\pi[$ are the co-latitude and longitude, respectively, and the map $\hat{\boldsymbol{M}}$ associates pairs $(\Theta,\Phi) \in [0,\pi]\times[0,2\pi[$ with unit vectors of $\mathbb{S}^2_X\mathscr{B}$. This permits to reinterpret the probability density distribution as a function $\hat{\wp} : [0,\pi] \times [0,2\pi[\to \mathbb{R}^+_0$ such that

$$\wp(\boldsymbol{M}) = \wp(\hat{\boldsymbol{M}}(\Theta,\Phi)) = \hat{\wp}(\Theta,\Phi). \tag{14}$$

The functional dependence of the probability density distribution on $\boldsymbol{M}$ must be consistent with the symmetries attributed to the material under study. This leads to some restrictions. In particular, due to the transverse isotropy, $\hat{\wp}$ should be independent of the longitude Φ, i.e., $\hat{\wp}(\Theta,\Phi) \equiv \hat{\wp}(\Theta) : [0,\pi] \to \mathbb{R}^+_0$.

By introducing a function f over $\mathbb{S}^2_X\mathscr{B}$, the directional average of f is defined by (see [15] for the notation)

$$\langle\!\langle f \rangle\!\rangle = \int_{\mathbb{S}^2_X\mathscr{B}} \wp(\boldsymbol{M})f(\boldsymbol{M}). \tag{15}$$

In general, f may represent a scalar-, a vector-, or a tensor-valued quantity. However, for the sake of simplicity, we will consider only scalars in the remainder of this section. In the following, f shall identify a constitutive function describing, for instance, the elasticity or the permeability of articular cartilage. Moreover, as we will see in Section 3, the dependence of such constitutive functions on the fibre orientation requires f to be an even function of $\boldsymbol{M}$, i.e., it holds $f(\boldsymbol{M}) = f(-\boldsymbol{M})$, for all $\boldsymbol{M} \in \mathbb{S}^2_X\mathscr{B}$. Since the probability density enjoys the same property, the product $\wp f$ is itself an even function of $\boldsymbol{M} \in \mathbb{S}^2_X\mathscr{B}$, which means that the directional average of f can also be performed by integrating on a half of $\mathbb{S}^2_X\mathscr{B}$ only. For instance, if $\wp$ and f are restricted to the northern hemisphere

$$\mathbb{S}^{2+}_X\mathscr{B} := \{\boldsymbol{M} \in T_X\mathscr{B} : \ \|\boldsymbol{M}\| = 1, \ \ \boldsymbol{M}.\boldsymbol{\mathcal{E}}_3 \geq 0\}, \quad (16)$$

then the directional average of f can be computed as

$$\langle\!\langle f \rangle\!\rangle = 2 \int_{\mathbb{S}^{2+}_X\mathscr{B}} \wp(\boldsymbol{M}) f(\boldsymbol{M}). \quad (17)$$

In order to be compliant with the normalisation condition, $\wp$ is usually written as

$$\wp = \frac{\mathfrak{p}}{\mathcal{Z}}, \quad \mathcal{Z} = \int_{\mathbb{S}^2_X\mathscr{B}} \mathfrak{p}(\boldsymbol{M}), \quad (18)$$

where $\mathfrak{p} : \mathbb{S}^2_X\mathscr{B} \to \mathbb{R}^+_0$ is the non-normalised density, and $\mathcal{Z}$ is referred to as the normalisation factor. In this case, by restricting $\mathfrak{p}$ to $\mathbb{S}^{2+}_X\mathscr{B}$, and introducing the additional quantities

$$\gamma := \mathfrak{p}_{|\mathbb{S}^{2+}_X\mathscr{B}} : \mathbb{S}^{2+}_X\mathscr{B} \to \mathbb{R}^+_0, \quad (19a)$$

$$\mathcal{Z}_+ := \int_{\mathbb{S}^{2+}_X\mathscr{B}} \gamma(\boldsymbol{M}) = \tfrac{1}{2}\mathcal{Z}, \quad (19b)$$

one can define the new probability density

$$\varPsi : \mathbb{S}^{2+}_X\mathscr{B} \to \mathbb{R}^+_0, \quad \varPsi = \frac{\gamma}{\mathcal{Z}_+} = 2\, \wp_{|\mathbb{S}^{2+}_X\mathscr{B}}, \quad (20)$$

and reformulate the average (17) as

$$\langle\!\langle f \rangle\!\rangle = \int_{\mathbb{S}^{2+}_X\mathscr{B}} \varPsi(\boldsymbol{M}) f(\boldsymbol{M}). \quad (21)$$

We emphasise that the procedure leading to (21) from (15) can be applied only when a given probability density $\wp$, that is naturally defined over $\mathbb{S}^2_X\mathscr{B}$, can be appropriately renormalised onto $\mathbb{S}^{2+}_X\mathscr{B}$ to obtain $\varPsi$. For example, this is the case of the von Mises distribution introduced in Section 3. However, we will also consider the case in which the probability density is defined only on $\mathbb{S}^{2+}_X\mathscr{B}$, and is not prolongated to $\mathbb{S}^2_X\mathscr{B}$ (this occurs, for example, when the pseudo-Gaussian distribution (35b) is used). In these situations, the directional average of a given physical quantity is defined by (21), which cannot be deduced from (15), and the probability density, being defined only on a hemisphere, cannot be claimed to enjoy any parity symmetry.

2.4 Balance laws and constitutive relations

In this section, we review the balance laws that are relevant for the poroelastic model of articular cartilage and the hypotheses on which it relies. The presentation follows that reported in [58]. The first assumption is that the mass-exchange processes occurring among the constituents of the tissue can be disregarded over the time-scales that characterise the experiments investigated in this work. Accordingly, in local form, the mass balance laws of the tissue's constituents are written as

$$D_{\mathrm{s}}(\phi_{0\mathrm{s}}\rho_0) + \phi_{0\mathrm{s}}\rho_0 \operatorname{div} \boldsymbol{v}_{\mathrm{s}} = 0, \quad (22a)$$

$$D_{\mathrm{s}}(\phi_{1\mathrm{s}}\rho_1) + \phi_{1\mathrm{s}}\rho_1 \operatorname{div} \boldsymbol{v}_{\mathrm{s}} = 0, \quad (22b)$$

$$D_{\mathrm{s}}(\phi_{\mathrm{f}}\rho_{\mathrm{f}}) + \phi_{\mathrm{f}}\rho_{\mathrm{f}} \operatorname{div} \boldsymbol{v}_{\mathrm{s}} + \operatorname{div}(\rho_{\mathrm{f}}\boldsymbol{q}) = 0, \quad (22c)$$

where ρ_0, ρ_1, and ρ_{f} are the mass densities of the matrix, fibres, and interstitial fluid, respectively, and $\boldsymbol{q} = \phi_{\mathrm{f}}(\boldsymbol{v}_{\mathrm{f}} - \boldsymbol{v}_{\mathrm{s}})$ is the filtration velocity of the fluid.

The second hypothesis is that ρ_0, ρ_1, and ρ_{f} are constant in space and time, which allows to divide the balance law of each constituent by the corresponding mass density. By multiplying the resulting expressions by J, and using (8)–(10), (22a)–(22c) become

$$\dot{\phi}_{0\mathrm{sR}} = 0, \quad (23a)$$

$$\dot{\phi}_{1\mathrm{sR}} = 0, \quad (23b)$$

$$\dot{\phi}_{\mathrm{fR}} + \operatorname{Div} \boldsymbol{Q} = 0. \quad (23c)$$

In (23a)–(23c), $\phi_{0\mathrm{sR}}$, $\phi_{1\mathrm{sR}}$, and ϕ_{fR} are the Piola transforms of $\phi_{0\mathrm{s}}$, $\phi_{1\mathrm{s}}$, and ϕ_{f}, respectively, and read

$$\phi_{\alpha\mathrm{sR}}(X) = J(X,t)\phi_{\alpha\mathrm{s}}(\chi(X,t),t), \quad \alpha \in \{0,1\}, \quad (24a)$$

$$\phi_{\mathrm{fR}}(X,t) = J(X,t)\phi_{\mathrm{f}}(\chi(X,t),t). \quad (24b)$$

Equations (23a) and (23b) imply that $\phi_{0\mathrm{sR}}$ and $\phi_{1\mathrm{sR}}$ are constant in time, which means that the Piola transform of the volumetric fraction of the solid phase as a whole, $\phi_{\mathrm{sR}} = \phi_{0\mathrm{sR}} + \phi_{1\mathrm{sR}}$, is constant in time, too. In particular, coherently with (24a), ϕ_{sR} is given by

$$\phi_{\mathrm{sR}}(X) = J(X,t)\phi_{\mathrm{s}}(\chi(X,t),t). \quad (25)$$

The results (24a) and (25) are equivalent to (22a) and (22b), respectively, and constrain $\phi_{0\mathrm{s}}$, $\phi_{1\mathrm{s}}$, and ϕ_{s} to vary as the reciprocal of the volumetric ratio. This means that the mass density of the solid phase, defined by the equality $\phi_{\mathrm{s}}\rho_{\mathrm{s}} = \phi_{0\mathrm{s}}\rho_0 + \phi_{1\mathrm{s}}\rho_1$, has zero substantial derivative. Consequently, the solid phase behaves as an incompressible material, even though J need not be constrained to be equal to 1. Moreover, by enforcing the saturation condition into (24b), ϕ_{fR} can be expressed as $\phi_{\mathrm{fR}} = J - \phi_{\mathrm{sR}}$, which yields $\dot{\phi}_{\mathrm{fR}} = \dot{J}$ and, from (23c),

$$\dot{J} + \operatorname{Div} \boldsymbol{Q} = 0. \quad (26)$$

The third hypothesis is that both inertial forces and external body forces applied to the tissue can be disregarded. Consequently, the momentum balance laws for the solid and fluid phase read

$$\operatorname{div}\boldsymbol{\sigma}_{\mathrm{s}} + \boldsymbol{m}_{\mathrm{s}} = \boldsymbol{0}, \tag{27a}$$
$$\operatorname{div}\boldsymbol{\sigma}_{\mathrm{f}} + \boldsymbol{m}_{\mathrm{f}} = \boldsymbol{0}, \tag{27b}$$

where $\boldsymbol{\sigma}_{\mathrm{s}}$ and $\boldsymbol{\sigma}_{\mathrm{f}}$ are the Cauchy stress tensors of the solid and fluid phase, respectively, and the internal body force $\boldsymbol{m}_k$, with $k = \mathrm{f}, \mathrm{s}$, represents the gain or loss of momentum of the αth phase due to the interactions with the other one. It should be noted that, since the matrix and the fibres share the same velocity, only one equation is written for the solid phase as a whole. Since the tissue as a whole experiences neither production nor loss of linear momentum, the body forces $\boldsymbol{m}_{\mathrm{s}}$ and $\boldsymbol{m}_{\mathrm{f}}$ must satisfy the closure condition $\boldsymbol{m}_{\mathrm{f}} + \boldsymbol{m}_{\mathrm{s}} = \boldsymbol{0}$. Thus, by summing together (27a) and (27b), one obtains

$$\operatorname{div}(\boldsymbol{\sigma}_{\mathrm{f}} + \boldsymbol{\sigma}_{\mathrm{s}}) = \boldsymbol{0}, \tag{28a}$$
$$\operatorname{div}\boldsymbol{\sigma}_{\mathrm{f}} + \boldsymbol{m}_{\mathrm{f}} = \boldsymbol{0}. \tag{28b}$$

The Piola transform of (28a) and (28b) is given by

$$\operatorname{Div}(\boldsymbol{P}_{\mathrm{f}} + \boldsymbol{P}_{\mathrm{s}}) = \boldsymbol{0}, \tag{29a}$$
$$\operatorname{Div}\boldsymbol{P}_{\mathrm{f}} + J\boldsymbol{m}_{\mathrm{f}} = \boldsymbol{0}, \tag{29b}$$

where $\boldsymbol{P}_k$, $k = \mathrm{f}, \mathrm{s}$, is the first Piola-Kirchhoff stress tensor of the kth phase and, with abuse of notation, $\boldsymbol{m}_{\mathrm{f}}$ in (29b) is expressed as a function of time and $X \in \mathscr{B}$. Equations (29a) and (29b) are obtained by multiplying (28a) and (28b) by J, and using the identities [47]

$$J(X,t)\operatorname{div}\boldsymbol{\sigma}_k(\chi(X,t),t) = \operatorname{Div}\boldsymbol{P}_k(X,t), \tag{30a}$$
$$\boldsymbol{P}_k(X,t) = J(X,t)\boldsymbol{\sigma}_k(\chi(X,t),t)\boldsymbol{F}^{-\mathrm{T}}(X,t). \tag{30b}$$

Hereafter, it is assumed that the fluid is macroscopically inviscid and that the solid phase is hyperelastic with respect to the configuration $\mathscr{B}$. Accordingly, $\boldsymbol{\sigma}_{\mathrm{f}}$ and $\boldsymbol{\sigma}_{\mathrm{s}}$ are expressed as [9,35]

$$\boldsymbol{\sigma}_{\mathrm{f}} = -\phi_{\mathrm{f}} p\, \boldsymbol{g}^{-1}, \tag{31a}$$
$$\boldsymbol{\sigma}_{\mathrm{s}} = -\phi_{\mathrm{s}} p\, \boldsymbol{g}^{-1} + \boldsymbol{\sigma}_{\mathrm{sc}}. \tag{31b}$$

In (31a) and (31b), p is the pore pressure, whereas $\boldsymbol{\sigma}_{\mathrm{sc}}$ is said to be the "constitutive part" of $\boldsymbol{\sigma}_{\mathrm{s}}$, since it is determined by the hyperelastic constitutive law

$$\boldsymbol{\sigma}_{\mathrm{sc}} = \hat{\boldsymbol{\sigma}}_{\mathrm{sc}}(\boldsymbol{F}) = \frac{1}{J}\boldsymbol{F}\left(2\frac{\partial \hat{W}}{\partial \boldsymbol{C}}(\boldsymbol{C})\right)\boldsymbol{F}^{\mathrm{T}}, \tag{32}$$

with the superimposed hat standing for "constitutive function", and $\hat{W}$ being the hyperelastic strain energy density function of the solid phase [31,58]. In (32) and in the following, $\boldsymbol{\sigma}_{\mathrm{f}}$, $\boldsymbol{\sigma}_{\mathrm{s}}$, and $\boldsymbol{\sigma}_{\mathrm{sc}}$ are regarded as a functions of time and points $X \in \mathscr{B}$. It should be noted that the pore pressure, p, cannot be determined constitutively, because the mass density of the fluid, ρ_{f}, is assumed to be constant, which implies that the fluid is regarded as incompressible. Rather, p constitutes, together with the motion of the solid phase, χ, one of the unknowns of the problem.

It can be proven that the momentum exchange rate, $\boldsymbol{m}_{\mathrm{f}}$, splits additively as $\boldsymbol{m}_{\mathrm{f}} = p\,\boldsymbol{g}^{-1}\operatorname{grad}\phi_{\mathrm{f}} + \boldsymbol{m}_{\mathrm{fd}}$, where $\boldsymbol{m}_{\mathrm{fd}}$ is the "dissipative part" of $\boldsymbol{m}_{\mathrm{f}}$ [9,35]. The term $\boldsymbol{m}_{\mathrm{fd}}$ can be expressed constitutively by supposing that Darcy's law is valid. Hence, $\boldsymbol{m}_{\mathrm{fd}}$ is written as a function of $\boldsymbol{F}$ and the filtration velocity $\boldsymbol{q}$. In particular, this function is assumed to be nonlinear in $\boldsymbol{F}$ and linear in $\boldsymbol{q}$. We set, thus, $\boldsymbol{m}_{\mathrm{fd}} = \hat{\boldsymbol{m}}_{\mathrm{fd}}(\boldsymbol{F},\boldsymbol{q}) = -\phi_{\mathrm{f}}\boldsymbol{g}^{-1}\boldsymbol{k}^{-1}\boldsymbol{q}$, where $\boldsymbol{k}$ is the permeability tensor of the medium. These results allow to rephrase the momentum balance law (28b) in terms of Darcy's law:

$$\boldsymbol{q} = -\boldsymbol{k}\operatorname{grad} p. \tag{33}$$

In the literature on hydrogeological porous media, $\boldsymbol{k}$ is usually referred to as *hydraulic conductivity*, and it is expressed as the ratio of the medium's *permeability* (in fact, a quantity depending on the structure of the pore space) to the fluid's viscosity [7]. In the present context, however, we prefer to stick to the nomenclature adopted in Biomechanics, in which $\boldsymbol{k}$ is known as "tissue's permeability", and depends both on the tissue's microstructure and the flow properties of the interstitial fluid.

By performing the Piola transform of (31a), (31b), and (33), the first Piola-Kirchhoff stress tensors $\boldsymbol{P}_{\mathrm{f}}$ and $\boldsymbol{P}_{\mathrm{s}}$, and the filtration velocity $\boldsymbol{Q}$ take on the form

$$\boldsymbol{P}_{\mathrm{f}} = -(J - \phi_{\mathrm{sR}})p\,\boldsymbol{g}^{-1}\boldsymbol{F}^{-\mathrm{T}}, \tag{34a}$$
$$\boldsymbol{P}_{\mathrm{s}} = -\phi_{\mathrm{sR}} p\,\boldsymbol{g}^{-1}\boldsymbol{F}^{-\mathrm{T}} + \boldsymbol{P}_{\mathrm{sc}}, \tag{34b}$$
$$\boldsymbol{Q} = -\boldsymbol{K}\operatorname{Grad} p, \tag{34c}$$

where $\boldsymbol{P}_{\mathrm{sc}} = J\boldsymbol{\sigma}_{\mathrm{sc}}\boldsymbol{F}^{-\mathrm{T}}$ is the constitutive part of the first Piola-Kirchhoff stress and $\boldsymbol{K} = J\boldsymbol{F}^{-1}\boldsymbol{k}\boldsymbol{F}^{-\mathrm{T}}$ is referred to as the tissue's "material permeability" [4,25].

To close the model, constitutive expressions for $\boldsymbol{P}_{\mathrm{sc}}$ and $\boldsymbol{K}$ are sought for. Since $\boldsymbol{P}_{\mathrm{sc}}$ is defined through the relation $\boldsymbol{P}_{\mathrm{sc}} = \boldsymbol{F}(2\partial_{\boldsymbol{C}}\hat{W}(\boldsymbol{C}))$, it can be determined by prescribing the strain energy density function $\hat{W}(\boldsymbol{C})$.

3 Constitutive model of Articular Cartilage

In the sequel, a cylindric sample of AC of height L and circular cross section will be used for the benchmark tests. The upper and lower boundaries of the sample represent, respectively, the articular surface of cartilage, and the surface at which it is attached to the subchondral bone [46]. The specimen is assumed to be transversely isotropic with respect to the axis of the cylinder, which thus coincides with $\boldsymbol{\xi}$. The direction of $\boldsymbol{\xi}$ is also said to be the "direction of the tissue depth" [58]. If the cartesian basis of orthonormal vectors $\{\boldsymbol{E}_A\}_{A=1}^3$ is chosen as the global reference frame for the whole sample, with its unit vectors emanating from the centre of the lower boundary, and $\boldsymbol{E}_3 \equiv \boldsymbol{\xi}$, then the coordinate associated with $\boldsymbol{\xi}$, X^3, can be normalised as $\xi = X^3/L$, thereby identifying the lower boundary with $\xi = 0$ and the upper one with $\xi = 1$.

Histological studies performed by Guilak et al. [32] show that AC can be roughly divided into three zones, which can be related to the variability of the fibre orientation with the axial (normalised) coordinate ξ [2, 50]. More specifically, the fibres appear to be almost parallel to the symmetry axis in the deep zone, randomly oriented in the middle zone, and parallel to the articular surface in the upper zone. This feature of the tissue's microstructure suggests the approximation according to which the material properties of AC vary with ξ, but are constant on each transverse plane. Consequently, we write $\hat{\Psi}(X, \Theta) \equiv \hat{\Psi}(\xi, \Theta)$ where, with a slight abuse of notation, we refer to $\hat{\Psi}$ as to a function of the axial coordinate ξ and the co-latitude Θ. Among other possible choices, we employ the pseudo-Gaussian distribution [17,30]

$$\hat{\Psi}_1(\xi, \cdot\,) : [0, \tfrac{\pi}{2}] \to \mathbb{R}_0^+, \tag{35a}$$

$$\hat{\Psi}_1(\xi, \Theta) = \frac{1}{\mathcal{Z}_{1+}(\xi)} \exp\left(-\frac{[\Theta - Q(\xi)]^2}{2[\sigma(\xi)]^2}\right), \tag{35b}$$

and the von Mises distribution

$$\hat{\Psi}_2(\xi, \cdot\,) : \left[0, \tfrac{\pi}{2}\right] \to \mathbb{R}_0^+, \tag{36a}$$

$$\hat{\Psi}_2(\xi, \Theta) = \frac{2}{\pi} \sqrt{\frac{b(\xi)}{2\pi}} \frac{\exp(b(\xi)[\cos(2\Theta) + 1])}{\operatorname{erfi}(\sqrt{2b(\xi)})}. \tag{36b}$$

Note that the von Mises distribution (36b) is already normalised over the hemisphere $\mathbb{S}_X^{2+}\mathscr{B}$. Indeed, given the probability density $\Psi_2(\xi, \cdot) : \mathbb{S}_X^{2+}\mathscr{B} \to \mathbb{R}_0^+$, such that $\Psi_2(\xi, \boldsymbol{M}) = \hat{\Psi}_2(\xi, \Theta)$, it holds that

$$\begin{aligned} 1 &= \int_{\mathbb{S}_X^{2+}\mathscr{B}} \Psi_2(\xi, \boldsymbol{M}) \\ &= 2\pi \int_0^{\pi/2} \hat{\Psi}_2(\xi, \Theta) \sin\Theta \, \mathrm{d}\Theta\,. \end{aligned} \tag{37}$$

In (35b), $\mathcal{Z}_{1+}(\xi)$ is the normalisation factor, $Q(\xi)$ is the most probable angle, and $[\sigma(\xi)]^2$ is the variance, whereas the parameter $b(\xi)$ in (36b) is referred to as concentration parameter. Here, we prescribe $Q(\xi)$ and $\sigma(\xi)$ as in [17], and we take $b(\xi)$ as an affine function of ξ, i.e.,

$$Q(\xi) = \frac{\pi}{2}\left[1 - \cos\left(\frac{\pi}{2}\left(-\frac{2}{3}\xi^2 + \frac{5}{3}\xi\right)\right)\right], \tag{38a}$$

$$\sigma(\xi) = 10^3[\xi(1-\xi)]^4 + 3 \cdot 10^{-3}, \tag{38b}$$

$$b(\xi) = -16\xi + 8. \tag{38c}$$

We remark that the general theory exposed in the following and the proposed algorithms, A1 and A2, hold for both choices of the probability density.

As shown in Figure 1, $Q(\xi)$ grows monotonically from Q(0) = 0 to $Q(1) = \pi/2$. Indeed, at the bone-cartilage interface, the most probable fibre alignment is along the direction of the symmetry axis, while at the articular surface fibres lie in the transverse plane and, due to transverse isotropy, they are randomly oriented on it. In terms of fibre alignment, the tissue experiences a "transition" between two ordered configurations (the one at $\xi = 0$ being more ordered than that at $\xi = 1$), passing through a highly disordered configuration. This is reflected by the standard deviation, σ, which tends towards zero (for simulation purposes, it is kept "small enough") for ξ approaching $\xi = 0$ and $\xi = 1$, and attains a global maximum at $\xi = 1/2$, where the randomness in the fibre orientation is maximal (i.e., in the limit of perfectly randomly oriented fibres, the variance should tend towards infinity). In the case of the von Mises probability density, the dispersion in the fibres' alignment is represented by the depth-dependent parameter $b(\xi)$, which is prescribed in (38c) to capture the arrangement of the collagen fibres sketched in Figure 1. In particular, since the concentration parameter describes fibres aligned vertically when it diverges positively, a random arrangement of fibres when it is zero, and fibres oriented horizontally when it diverges negatively, we take $b(\xi)$ as a monotonously increasing function of $\xi \in [0, 1]$ and, as done in previous works [58,34], we assume that its range is $[-8, 8]$. Hereafter, we shall indicate the probability density by $\hat{\Psi}$ whenever there is no need to specify whether it has to be $\hat{\Psi}_1$ or $\hat{\Psi}_2$.

3.1 Constitutive Model

Coherently with the model put forward in [18,19,21,24, 43], $\hat{W}$ is specified by superimposing the strain energy density of the matrix, $\hat{W}_0$, with that of the fibres, $\hat{W}_{\mathrm{e}}$. Moreover, following [19], a penalty term, is added to account for the incompressibility of the solid phase at compaction:

$$\hat{W}(\boldsymbol{C}) = \phi_{\mathrm{sR}}\hat{U}(J) + \phi_{0\mathrm{sR}}\hat{W}_0(\boldsymbol{C}) + \phi_{1\mathrm{sR}}\hat{W}_{\mathrm{e}}(\boldsymbol{C}). \tag{39}$$

The term $\hat{U}$ depends on $\boldsymbol{C}$ only through the volumetric ratio, $J = \sqrt{\det(\boldsymbol{C})}$, and takes on the form [19]

$$\hat{U}(J) = \mathcal{H}(J_{\text{crit}} - J)\frac{(J - J_{\text{crit}})^{2q}}{(J - \phi_{\text{sR}})^r}, \tag{40}$$

where $\mathcal{H}$ is the Heaviside function, $J_{\text{crit}} \in]\phi_{\text{sR}}, 1]$ is a "critical" value of the volumetric ratio, below which the potential $\hat{U}$ is switched on, while $q \geq 2$ and $r \in]0, 1]$ are material parameters (q is an integer). In this work, the strain energy density of the matrix, $\hat{W}_0$, is assumed to be of Neo-Hookean type [11], i.e.,

$$\begin{aligned}\hat{W}_0(\boldsymbol{C}) =& \tfrac{1}{8}\lambda_0 \left(\ln[\det(\boldsymbol{C})]\right)^2 - \tfrac{1}{2}\mu_0 \ln[\det(\boldsymbol{C})] \\ &+ \tfrac{1}{2}\mu_0 \left(\boldsymbol{G}^{-1}:\boldsymbol{C} - 3\right),\end{aligned} \tag{41}$$

with λ_0 and μ_0 being the Lamé first modulus and the shear modulus of the matrix, respectively. Nevertheless, other choices of $\hat{W}_0$ are possible. Usually, for articular cartilage, the Holmes-Mow strain energy is used [36]. The strain energy density associated with the fibres, $\hat{W}_{\text{e}}$, is said to be the "*ensemble fibre potential*" [20], and may be written as (see [18–20, 22] for details)

$$\begin{aligned}\hat{W}_{\text{e}}(\boldsymbol{C}) &= \hat{W}_{1\text{i}}(\boldsymbol{C}) + \hat{W}_{1\text{a}}(\boldsymbol{C}) \\ &= \hat{W}_{1\text{i}}(\boldsymbol{C}) + \int_{\mathbb{S}^{2+}_X \mathscr{B}} \Psi(\boldsymbol{M})\hat{w}_{1\text{a}}(\boldsymbol{C}, \boldsymbol{M}).\end{aligned} \tag{42}$$

In (42), $\hat{W}_{1\text{i}}$ and $\hat{W}_{1\text{a}}$ are the isotropic and the anisotropic contributions of the fibres to the overall strain energy density. More specifically, $\hat{W}_{1\text{i}}$ is assumed to have the same functional form as $\hat{W}_0$, the only difference being in the elastic constants, which are given by λ_1 and μ_1 in the case of $\hat{W}_{1\text{i}}$. The summand $\hat{W}_{1\text{a}}$, instead, is defined by the integral on the right-hand-side of (42), and is constructed in two steps: For each $X \in \mathscr{B}$, one considers the anisotropic strain energy density $\hat{w}_{1\text{a}}(\boldsymbol{C}, \boldsymbol{M})$, which is associated with the fibres oriented along the unit vector $\boldsymbol{M}$ emanating from X. Then, $\hat{w}_{1\text{a}}(\boldsymbol{C}, \boldsymbol{M})$ is multiplied by the probability density $\Psi(\boldsymbol{M})$ of finding a family of fibres aligned along $\boldsymbol{M}$, and the result is integrated over the material unit hemisphere $\mathbb{S}^{2+}_X \mathscr{B}$. Here, $\hat{w}_{1\text{a}}(\boldsymbol{C}, \boldsymbol{M})$ is chosen as

$$\hat{w}_{1\text{a}}(\boldsymbol{C}, \boldsymbol{M}) = \mathcal{H}(I_4 - 1)\tfrac{c}{2}[I_4 - 1]^2, \tag{43}$$

where the short-hand notation

$$I_4 \equiv I_4(\boldsymbol{C}, \boldsymbol{M}) := \text{tr}[\boldsymbol{C}(\boldsymbol{M} \otimes \boldsymbol{M})] = \text{tr}[\boldsymbol{C}\boldsymbol{A}] \tag{44}$$

has been introduced to express the fourth invariant of the deformation, c is a material parameter, and $\mathcal{H}$ is the Heaviside function. The fourth invariant extracts the component of $\boldsymbol{C}$ in the direction of $\boldsymbol{M}$, and expresses whether the fibre oriented along $\boldsymbol{M}$ is stretched, i.e., $I_4 > 1$, contracted, i.e., $I_4 < 1$, or neutral, in which case $I_4 = 1$. The Heaviside function selects only stretched fibres as contributors to the ensemble fibre potential. The tensor $\boldsymbol{A} = \boldsymbol{M} \otimes \boldsymbol{M}$ is referred to as structure tensor.

When the penalty term $\hat{U}(J)$ is not active, the constitutive part of the first Piola-Kirchhoff stress tensor, $\boldsymbol{P}_{\text{sc}} = \hat{\boldsymbol{P}}_{\text{sc}}(\boldsymbol{F})$, is given by

$$\begin{aligned}\hat{\boldsymbol{P}}_{\text{sc}}(\boldsymbol{F}) =& \tfrac{1}{2}\lambda \ln[\det(\boldsymbol{C})]\boldsymbol{g}^{-1}\boldsymbol{F}^{-\text{T}} + \mu\boldsymbol{F}\left(\boldsymbol{G}^{-1} - \boldsymbol{C}^{-1}\right) \\ &+ \boldsymbol{F}\boldsymbol{S}_{\text{a}},\end{aligned} \tag{45}$$

where $\lambda := \phi_{0\text{sR}}\lambda_0 + \phi_{1\text{sR}}\lambda_1$ and $\mu := \phi_{0\text{sR}}\mu_0 + \phi_{1\text{sR}}\mu_1$ are the elastic moduli of the solid phase, and $\boldsymbol{S}_{\text{a}}$ is the anisotropic part of the constitutive second Piola-Kirchhoff stress tensor, i.e.,

$$\boldsymbol{S}_{\text{a}} = 2\phi_{1\text{sR}}c \int_{\mathbb{S}^{2+}_X \mathscr{B}} \Psi(\boldsymbol{M})\mathcal{H}(I_4 - 1)[I_4 - 1]\boldsymbol{A}. \tag{46}$$

To complete the constitutive framework, the tissue's permeability has to be specified. In this work, we use the model presented in [19, 58], which extends the results obtained in [21, 22] to the case of finite deformations. In [21, 22], a Representative Elementary Volume (REV) is claimed to exist, which consists of one segment of fibre, the matrix, and the fluid. The REV permeability is determined through an upscaling procedure, based on techniques put forward in [42, 48, 51, 53]. By construction, it depends on the direction of the fibre in whose neighbourhood the REV is constructed. Thus, the permeability of the tissue, $\boldsymbol{k}$, is computed by performing the directional average of the REV permeability. Hence, the Piola transform of $\boldsymbol{k}$ yields the "material permeability", $\boldsymbol{K}$, whose constitutive form is given by

$$\begin{aligned}\boldsymbol{K} = \hat{\boldsymbol{K}}(\boldsymbol{F}) =& \hat{k}_0(J)\frac{(J - \phi_{1\text{sR}})^2}{J}\boldsymbol{C}^{-1} \\ &+ \hat{k}_0(J)\frac{(J - \phi_{1\text{sR}})\phi_{1\text{sR}}}{J}\hat{\boldsymbol{Z}}(\boldsymbol{C}),\end{aligned} \tag{47}$$

where the scalar permeability $\hat{k}_0(J)$ is defined on the basis of experimental data, and

$$\boldsymbol{Z} = \hat{\boldsymbol{Z}}(\boldsymbol{C}) := \int_{\mathbb{S}^{2+}_X \mathscr{B}} \Psi(\boldsymbol{M})\frac{\boldsymbol{M} \otimes \boldsymbol{M}}{I_4}. \tag{48}$$

According to the Holmes-Mow permeability model, $\hat{k}_0(J)$ reads

$$\hat{k}_0(J) = k_{0\text{R}} \left[\frac{J - \phi_{\text{sR}}}{1 - \phi_{\text{sR}}}\right]^\kappa \exp\left(\frac{M}{2}[J^2 - 1]\right), \tag{49}$$

where $k_{0\text{R}}$, κ, and M are material parameters generally depending on the point of the tissue at which they are evaluated. Note that a different formulation of the deformation-dependent permeability in anisotropic media was proposed in [4].

3.2 Model Equations

By exploiting the constitutive expressions (45) and (47), the balance laws (26) and (29a) become

$$\dot{J} + \mathrm{Div}\left(-\hat{\boldsymbol{K}}(\boldsymbol{F})\,\mathrm{Grad}\,p\right) = 0, \tag{50a}$$

$$\mathrm{Div}\left(-Jp\,\boldsymbol{g}^{-1}\boldsymbol{F}^{-\mathrm{T}} + \hat{\boldsymbol{P}}_{\mathrm{sc}}(\boldsymbol{F})\right) = \boldsymbol{0}. \tag{50b}$$

Equations (50a) and (50b) constitute the set of coupled partial differential equations that have to be solved to determine the motion of the solid phase, χ, and the pressure, p. We remark that the terms in parentheses in (50b) express the overall first Piola-Kirchhoff stress tensor $\hat{\boldsymbol{P}}(p,\boldsymbol{F}) := -Jp\boldsymbol{g}^{-1}\boldsymbol{F}^{-\mathrm{T}} + \hat{\boldsymbol{P}}_{\mathrm{sc}}(\boldsymbol{F})$ as a function of pressure and deformation. We emphasise that, since $\boldsymbol{P}_{\mathrm{sc}} = \hat{\boldsymbol{P}}_{\mathrm{sc}}(\boldsymbol{F})$ and $\boldsymbol{K} = \hat{\boldsymbol{K}}(\boldsymbol{F})$ depend solely on $\boldsymbol{F}$, $\hat{\boldsymbol{P}}(p,\boldsymbol{F})$ is an affine function of p, and Darcy's law (34c) constitutes a linear relation between $\boldsymbol{Q}$ and p, through $\mathrm{Grad}\,p$. Moreover, the model equations (50a) and (50b) are nonlinear in χ because they feature $J = \det(\boldsymbol{F})$, and also because $\hat{\boldsymbol{P}}_{\mathrm{sc}}(\boldsymbol{F})$ and $\hat{\boldsymbol{K}}(\boldsymbol{F})$ depend on $\boldsymbol{F}$ in nonlinear way.

The approximated solution to (50a) and (50b) is usually sought for by having recourse to Finite Element methods. For example, in the case of zero Neumann boundary conditions, and non-zero Dirichlet boundary conditions, the following weak formulation [27,31] applies

$$\mathfrak{F}_p := -\int_{\mathscr{B}} \left\{(\mathrm{Grad}\,\tilde{p})\hat{\boldsymbol{K}}(\boldsymbol{F})\mathrm{Grad}\,p + \tilde{p}\dot{J}\right\} = 0, \tag{51a}$$

$$\mathfrak{F}_\chi := \int_{\mathscr{B}} \hat{\boldsymbol{P}}(p,\boldsymbol{F}) : \boldsymbol{g}\mathrm{Grad}\tilde{\boldsymbol{u}} = 0, \tag{51b}$$

where $\tilde{p}$ and $\tilde{\boldsymbol{u}}$ are the test functions of the problem, and belong to the sets

$$\tilde{\mathscr{P}} = \{\tilde{p} \in H^1_0(\mathscr{B}) : \ \tilde{p}_{|\Gamma^p_{\mathrm{D}}} = 0\}, \tag{52a}$$

$$\tilde{\mathscr{V}} = \{\tilde{\boldsymbol{u}} \in \boldsymbol{H}^1_0(\mathscr{B}) : \ \tilde{\boldsymbol{u}}_{|\Gamma^\chi_{\mathrm{D}}} = \boldsymbol{0}\}, \tag{52b}$$

with Γ^p_{D} and Γ^χ_{D} being, respectively, the portions of the boundary of $\mathscr{B}$ on which Dirichlet conditions are imposed. Physically, $\tilde{p}$ and $\tilde{\boldsymbol{u}}$ represent a virtual pressure and a virtual velocity, respectively. Note that the functionals $\mathfrak{F}_p =: \hat{\mathfrak{F}}_p(\chi,p,\tilde{p})$ and $\mathfrak{F}_\chi := \hat{\mathfrak{F}}_\chi(\chi,p,\tilde{\boldsymbol{u}})$ are linear in $\tilde{p}$ and $\tilde{\boldsymbol{u}}$, affine in p, and highly nonlinear in χ.

As pointed out in [16,34], the main difficulty in solving (51a) and (51b) is due to the constitutive laws expressing $\hat{\boldsymbol{P}}_{\mathrm{sc}}(\boldsymbol{F})$ and $\hat{\boldsymbol{K}}(\boldsymbol{F})$, which necessitate the solution of integrals of functions, defined over $\mathbb{S}^{2+}_X\mathscr{B}$, for which the deformation cannot be factorised (cf. (45) and (47)). This is due to the presence of the Heaviside function of $(I_4(\boldsymbol{C},\boldsymbol{M})-1)$ in the case of $\hat{\boldsymbol{P}}_{\mathrm{sc}}(\boldsymbol{F})$, and to the division by $I_4(\boldsymbol{C},\boldsymbol{M})$ in the case of $\hat{\boldsymbol{K}}(\boldsymbol{F})$. To circumvent these problems, dedicated algorithms are required. The rest of this work is devoted to a comparative study of some of these algorithms and to the evaluation of their features.

4 The Spherical Design Algorithm (SDA)

Let f be any (scalar, vector, or tensor) function defined over $\mathbb{S}^{2+}_X\mathscr{B}$. By using the identification (13), it holds that $f(\boldsymbol{M}) = \hat{f}(\Theta,\Phi)$ for all $\boldsymbol{M} \in \mathbb{S}^{2+}_X\mathscr{B}$, and $(\Theta,\Phi) \in \mathscr{D} = [0,\pi/2]\times[0,2\pi]$. If f is integrable over $\mathbb{S}^{2+}_X\mathscr{B}$, one can write

$$\int_{\mathbb{S}^{2+}_X\mathscr{B}} f(\boldsymbol{M}) = \iint_{\mathscr{D}} \hat{f}(\Theta,\Phi)\sin(\Theta)\mathrm{d}\Theta\mathrm{d}\Phi. \tag{53}$$

The Spherical t-Design [33] is a numerical method used to solve integrals of the same type as (53). After selecting two positive integers, m and n, and a proper set of pairs $\mathcal{X}_{ij} = (\Theta_i,\Phi_j) \in \mathscr{D}$, with $i = 1,\dots,m$ and $j = 1,\dots,n$, the integrals in (53) are approximated by

$$\begin{aligned}\iint_{\mathscr{D}} \hat{f}(\Theta,\Phi)\sin(\Theta)\mathrm{d}\Theta\mathrm{d}\Phi &\simeq \sum_{i=1}^{m}\sum_{j=1}^{n} w(\mathcal{X}_{ij})\hat{f}(\mathcal{X}_{ij}) \\ &= \frac{2\pi}{N}\sum_{i=1}^{m}\sum_{j=1}^{n}\hat{f}(\mathcal{X}_{ij}),\end{aligned} \tag{54}$$

with $N = mn$. Formula (54) is exact when $f(\boldsymbol{M})$ is a polynomial of degree t and $N = mn$ is a sufficiently high number of integration points [38]. Here, m denotes the dimension of the set of co-latitudes, whereas n stands for the dimension of the set of longitudes. It is worthwhile to notice that the factor $2\pi/N$ is the Nth part of the area of the surface of the unit hemisphere, and represents the area of a generic element of the grid covering $\mathscr{D}$. Since, for every $X \in \mathscr{B}$, each $\mathcal{X}_{ij} \in \mathscr{D}$ corresponds univocally to the unit vector $\boldsymbol{M}_{ij} = \hat{\boldsymbol{M}}(\mathcal{X}_{ij}) \in \mathbb{S}^{2+}_X\mathscr{B}$ and, thus, to the point Y_{ij} on the surface of the unit hemisphere, such that $Y_{ij} - X = \boldsymbol{M}_{ij}$, the grid covering $\mathscr{D}$ is mapped onto the surface of the unit hemisphere.

We remark that the SDA relies on the fact that, if the integration points are properly chosen, the weights $w(\mathcal{X}_{ij})$ in (54) are all equal to $\frac{2\pi}{N}$ for each point $\mathcal{X}_{ij}$, with $i = 1,\dots,m$ and $j = 1,\dots,n$. For other choices of the integration points, instead, non-trivial weights should be determined [8,12].

4.1 Proper choice of the integration points

The first important numerical issue related to the SDA is the appropriate choice of the discrete set of points in the domain $\mathscr{D}$. As shown in Figure 2, if we pick the points $\mathcal{X}_{ij}$, $i = 1, \dots, m$, $j = 1, \dots, n$, homogeneously in $\mathscr{D}$, they cluster close to the poles, as the integral measure depends on $\sin(\Theta)$. To skip this problem, we perform the change of variables [59],

$$\Theta = \operatorname{acos}(2v - 1), \quad \Phi = 2\pi u, \quad (v, u) \in \mathscr{E}, \tag{55}$$

with $\mathscr{E} = \left[\frac{1}{2}, 1\right] \times [0, 1]$. Clearly, the area of the surface of the unit hemisphere is preserved by (55), i.e.,

$$|\mathbb{S}^{2+}_X \mathscr{B}| = \iint_{\mathscr{D}} \sin(\Theta)\mathrm{d}\Theta\mathrm{d}\Phi = 4\pi \iint_{\mathscr{E}} \mathrm{d}v\mathrm{d}u = 2\pi, \tag{56}$$

and the integrals (53) and (54) can be rephrased as

$$\begin{aligned}\int_{\mathbb{S}^{2+}_X \mathscr{B}} f(\boldsymbol{M}) &= 4\pi \iint_{\mathscr{E}} \tilde{f}(v, u)\, \mathrm{d}v\mathrm{d}u \\ &\simeq \frac{2\pi}{N} \sum_{i=1}^{m} \sum_{j=1}^{n} \tilde{f}(v_i, u_j).\end{aligned} \tag{57}$$

Hereafter, we say that points chosen according to (55) are "equidistributed" in the sense that, quoting from [59], "*any small area on the* [hemi]*sphere is expected to contain the same number of points*". A number of suitable sets of points for the Spherical t-Design has been produced by Sloane [38], and is freely available online. We refer to such integration points as to "Sloane points". We remark, however, that any set of "Sloane points", hereafter denoted by $\mathcal{S}$, is defined as a discrete subset of $[0, \pi] \times [0, 2\pi]$. Thus, to apply the approximation formula (54) (or (57), in the case of equidistributed points), it is necessary to determine a subset $\mathcal{S}' \subset \mathcal{S}$ of Sloane points such that

$$\begin{aligned}\mathcal{S}' =& \{\mathcal{X}_{ij} \in \mathcal{S} |\ 0 \le \Theta_i \le \tfrac{\pi}{2}, \\ & i = 1, ..., m,\ j = 1, ..., n\}\end{aligned} \tag{58}$$

(and its counterpart in $\mathscr{E}$, if (57) is invoked). In the following, we shall calculate the directional averages featuring in the expressions of $\boldsymbol{Z}$ and $\boldsymbol{S}_{\mathrm{a}}$ by using $\mathcal{S}'$ in (54). For example, in the case of $\boldsymbol{Z}$, we obtain

$$\begin{aligned}\boldsymbol{Z} &= \int_{\mathbb{S}^{2+}_X \mathscr{B}} \Psi(\boldsymbol{M}) \frac{\boldsymbol{M} \otimes \boldsymbol{M}}{I_4} \\ &\approx \frac{2\pi}{N} \sum_{i=1}^{m} \sum_{j=1}^{n} \hat{\Psi}(\mathcal{X}_{ij}) \frac{\hat{\boldsymbol{M}}(\mathcal{X}_{ij}) \otimes \hat{\boldsymbol{M}}(\mathcal{X}_{ij})}{I_4(\boldsymbol{C}, \hat{\boldsymbol{M}}(\mathcal{X}_{ij}))},\end{aligned} \tag{59}$$

where $\mathcal{X}_{ij} \in \mathcal{S}'$ for all $i = 1, \dots, m$, and $j = 1, \dots, n$, and $\hat{\Psi}$ can be either the pseudo-Gaussian distribution $\hat{\Psi}_1$ in (35b) or the von Mises distribution $\hat{\Psi}_2$ in (36b). As we will show in discussing the results of the present work, depending on the type of function to be averaged, a given set of points of $\mathcal{S}'$ may, or may not, deliver acceptable results.

As it will be seen in the computation of the tissue's permeability (cf. Figure 3), an appropriate choice of the integration points strongly influences the evaluation of the integrals over $\mathbb{S}^{2+}_X \mathscr{B}$ by means of the SDA.

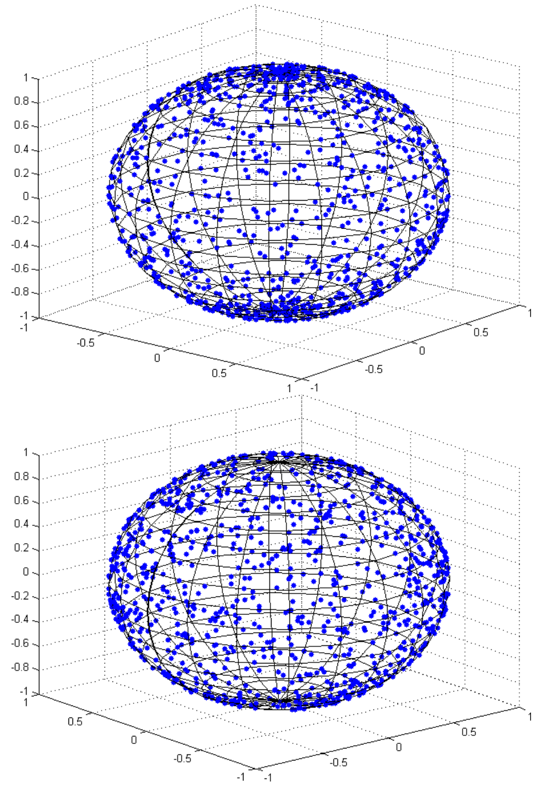

Fig. 2 Points $\mathcal{X}_{ij} \in \mathscr{D}$ mapped onto the surface of the sphere (blue dots). (a) Points corresponding to homogeneously chosen $\mathcal{X}_{ij}$. (b) Points corresponding to $\mathcal{X}_{ij}$ chosen according to (55).

4.2 Preliminary test of the SDA

The SDA, as sketched in algorithm A1, is often used for the numerical evaluation of the integrals over $\mathbb{S}^{2+}_X \mathscr{B}$ that appear in the constitutive expressions of stress and permeability (cf. (45) and (47), respectively). It comes into play after (51a) and (51b) are discretised in time and space, and is invoked within each time step and each iteration of the adopted linearisation procedure. As shown in A1, three nested loops have to be performed to run the SDA: One of them is on the chosen grid vertices, while the second two refer to the set of points $\mathcal{X}_{ij}$ selected in $\mathscr{D}$. In this work, the SDA is compared with an integration scheme available in Matlab, which has been sketched in the algorithms A2 and A3. In particular, we specify in A3 the functions used for the implementation of A2.

The Heaviside function in (46) is taken into account by means of an `If` cycle both in the SDA routine (line 18 of algorithm A1) and in the Matlab subroutine "STRESS" (line 11 of algorithm A2). Indeed, since for a given Cauchy-Green deformation tensor $\boldsymbol{C}$, the integrand of (46) is different from zero only if $I_4 > 1$, only stretched fibres contribute to the stress $\boldsymbol{S}_{\mathrm{a}}$, which can thus be computed as (recall that $\boldsymbol{A} = \boldsymbol{M} \otimes \boldsymbol{M}$)

$$\boldsymbol{S}_{\mathrm{a}} = 2\phi_{1\mathrm{sR}} c \int_{\mathbb{H}_X(\boldsymbol{C})} \Psi(\boldsymbol{M})[I_4 - 1]\boldsymbol{A}, \tag{60}$$

where the integration domain $\mathbb{H}_X(\boldsymbol{C})$ is given by

$$\mathbb{H}_X(\boldsymbol{C}) = \left\{\boldsymbol{M} \in \mathbb{S}^{2+}_X\mathscr{B} \,|\, \boldsymbol{C} : (\boldsymbol{M} \otimes \boldsymbol{M}) > 1\right\}. \tag{61}$$

We remark that the integrand of (60) is bounded and $C^\infty(\mathbb{H}_X(\boldsymbol{C}))$, for all $\boldsymbol{C}$. The numerical evaluation of (60), performed by means of the SDA, yields

$$\begin{aligned} \boldsymbol{S}_{\mathrm{a}} &= 2\phi_{1\mathrm{sR}} c \int_{\mathbb{H}_X(\boldsymbol{C})} \Psi(\boldsymbol{M})[I_4 - 1]\boldsymbol{A} \\ &\approx 2\phi_{1\mathrm{sR}} c \left(\tfrac{2\pi}{N} \sum_{ij}{}' \hat{\Psi}(\mathcal{X}_{ij})[\hat{I}_4(\mathcal{X}_{ij}) - 1]\hat{\boldsymbol{A}}(\mathcal{X}_{ij}) \right), \end{aligned} \tag{62}$$

where $\hat{\boldsymbol{A}}(\mathcal{X}_{ij}) = \hat{\boldsymbol{M}}(\mathcal{X}_{ij}) \otimes \hat{\boldsymbol{M}}(\mathcal{X}_{ij})$, and $\sum'_{ij}$ means that the sum is performed only for the values of i and j such that $\boldsymbol{C} : \hat{\boldsymbol{A}}(\mathcal{X}_{ij}) > 1$.

In this preliminary set of tests that we present, we investigate the reliability and the convergence of the SDA in response to the chosen set of integration points only, i.e., without implementing it in any Finite Element software. For this purpose, we consider the undeformed state of the tissue, in which it holds that $\boldsymbol{C} = \boldsymbol{G}$, $\boldsymbol{Z} = \boldsymbol{Z}_0 \equiv \hat{\boldsymbol{Z}}(\boldsymbol{G})$ (see (48)), and the stress tensor $\boldsymbol{S}_{\mathrm{a}}$ vanishes identically. Indeed, since $\boldsymbol{M}$ is a unit vector in the norm induced by $\boldsymbol{G}$, it holds that $I_4(\boldsymbol{G}, \boldsymbol{M}) = \mathrm{tr}[\boldsymbol{G}(\boldsymbol{M} \otimes \boldsymbol{M})] = 1$. Hence, $\boldsymbol{Z}_0$ can be evaluated as

$$\boldsymbol{Z}_0 = \iint_{\mathscr{D}} \hat{\Psi}(\xi, \Theta)\hat{\boldsymbol{A}}(\Theta, \Phi)\sin(\Theta)\mathrm{d}\Theta\mathrm{d}\Phi, \tag{63}$$

with $\hat{\boldsymbol{A}}(\Theta, \Phi) = \hat{\boldsymbol{M}}(\Theta, \Phi) \otimes \hat{\boldsymbol{M}}(\Theta, \Phi)$. We remark that $\boldsymbol{Z}_0$ is the averaged structure tensor. By expressing $\boldsymbol{M}$ as in (13), the components of $\boldsymbol{Z}_0$ become

$$(\boldsymbol{Z}_0)^{11} = (\boldsymbol{Z}_0)^{22} = \pi \int_0^{\pi/2} \hat{\Psi}(\xi, \Theta)[\sin(\Theta)]^3\mathrm{d}\Theta, \tag{64a}$$

$$(\boldsymbol{Z}_0)^{12} = (\boldsymbol{Z}_0)^{13} = (\boldsymbol{Z}_0)^{23} = 0, \tag{64b}$$

$$(\boldsymbol{Z}_0)^{33} = 1 - 2(\boldsymbol{Z}_0)^{11}. \tag{64c}$$

Since the deformation is not involved in this calculation, the evaluation of $(\boldsymbol{Z}_0)^{11}$ need not be coupled with the FE code, and serves as a preliminary analysis of the reliability of the SDA, thereby helping understand how the considered quadrature methods work. We compute $(\boldsymbol{Z}_0)^{11}$ by using both the SDA and the algorithm A2, and compare the results delivered by the two procedures.

It must be noticed that, in (64a), the integration with respect to Φ is computed exactly. Thus, only the integral with respect to Θ needs to be approximated. This is done by invoking the SDA and the Matlab routine.

As anticipated in section 4.1, and shown in Figure 3, if the values of Θ and Φ are taken homogeneously, the corresponding points on the unit hemisphere gather in the neighbourhood of the poles, and the radial component $(\boldsymbol{Z}_0)^{11}$ of the averaged structure tensor produced by the SDA (cf. algorithm A1) does not converge to the effective value of the integral (black, bold curve in Figure 3, evaluated by means of A2). The same considerations apply to the axial component $(\boldsymbol{Z}_0)^{33}$. Note that the points on the hemisphere corresponding to a homogeneous distribution of pairs $(\Theta, \Phi) \in \mathscr{D}$ are also said to be *equispaced*. We remark that the arrow crossing the curves in Figure 3 indicates the direction of ascending m. We see that, by increasing the value of m, the result of the numerical computation of (64a), done by means of the algorithm A1, converges to the one obtained with the algorithm A2, if *equidistributed* points are used to discretise the integration domain.

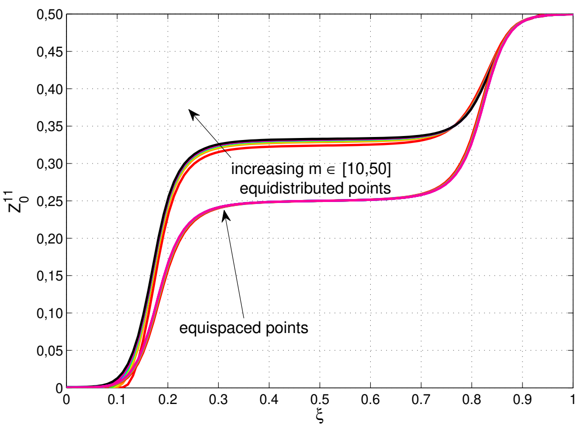

Fig. 3 Preliminary results of the algorithms A1 and A2 for the undeformed configuration. The solutions obtained by means of equispaced and equidistributed points are compared with the numerical outcome of the routine A2 (see also [22] for comparison).

In Figure 4, we show the results of the calculation of $(\boldsymbol{Z}_0)^{11}$ as in (64a) according to the numerical integration scheme A2 and to different sets of integration points used for the SDA. The first two sets are $\mathcal{S}'_{120} \subset \mathcal{S}_{240}$ and $\mathcal{S}'_{21} \subset \mathcal{S}_{41}$. They represent the subsets of the spherical designs $\mathcal{S}_{240}$ and $\mathcal{S}_{41}$ comprising 240 and 41 points, respectively [38], and obtained by selecting the pairs $\mathcal{X}_{ij} = (\Theta_i, \Phi_j)$, with $\Theta_i \in [0, \frac{\pi}{2}]$ and $\Phi_j \in [0, 2\pi]$. In fact, the spherical designs in [38] are conceived to perform the quadrature over $\mathbb{S}^2_X\mathscr{B}$, whereas we need to integrate over $\mathbb{S}^{2+}_X\mathscr{B}$, only. Three sets of equidistributed points, with $m = 10, 30, 50$, respectively, have been considered. Moreover, in this work, we propose and test a further set of points distributed as shown below

$$\Theta \in \mathcal{I} = \left\{0, \frac{\pi}{6}, \frac{\pi}{4}, \frac{\pi}{3}, \frac{2\pi}{5}, \frac{\pi}{2}\right\}, \tag{65a}$$

$$\Phi \in \mathcal{J} = \left\{0, \frac{\pi}{4}, \frac{\pi}{2}, \frac{3\pi}{4}, \pi, \frac{5\pi}{4}, \frac{3\pi}{2}, \frac{7\pi}{4}\right\}. \tag{65b}$$

The set $\mathcal{I} \times \mathcal{J} \subset \mathscr{D}$ consists of 48 points. However, by combining each Θ in (65a) with all the longitudes Φ in (65b), and noticing that for $\Theta = 0$ all directions defined by varying Φ "condense" in the north pole, the set $\mathcal{I} \times \mathcal{J}$ determines only 41 different elements of $\mathbb{S}^{2+}_X \mathscr{B}$.

In Figure 4a we can see that, if the pseudo-Gaussian distribution is used, i.e., if it holds $\hat{\Psi} = \hat{\Psi}_1$ for all the sets of points discretising the hemisphere, the results of the numerical integration of (64a) are in good agreement with those of the Matlab integration. In Figure 4b, we show the same results as in Figure 4a, but obtained by employing the von Mises probability density distribution, i.e., for $\hat{\Psi} = \hat{\Psi}_2$. In this case, we see that the set $\mathcal{S}'_{120}$ captures better the Matlab curve, and that, in general, the other sets of points fail for positive and increasing values of the concentration parameter b (we recall that b describes the dispersion of the fibres from the direction of most probable alignment). For example, this can be deduced by inspecting Figure 4b for $\xi = 0$, which corresponds to $b(0) = 8$. This inaccuracy could be attributed to the fact that the performance of some spherical designs deteriorates when the denominator of $\hat{\Psi}_2$ is sufficiently big. For instance, at $b(0) = 8$, $\mathrm{erfi}(\sqrt{2b(0)})$ returns a value that is about $1 \cdot 10^6$.

In Figure 5, we reported the integral error of the SDA with respect to the Matlab integration

$$err_{\mathrm{int}} = \int_0^1 \left|\left[(\boldsymbol{Z}_0)^{11}\right]_{\mathrm{SDA}} - \left[(\boldsymbol{Z}_0)^{11}\right]_{\mathrm{Matlab}}\right| \mathrm{d}\xi, \tag{66}$$

which is computed numerically by means of a trapezoidal quadrature formula. The orange, green, and magenta circles in the figure represent err_{int} in the discretisation of (64a) by means of $\mathcal{S}'_{21}$, $\mathcal{S}'_{120}$, and the new set $\mathcal{I} \times \mathcal{J}$, respectively, and for $\hat{\Psi} = \hat{\Psi}_1$. From Figure 5, we notice that the error in the computation with equidistributed points decreases exponentially with increasing m (we recall that m is the number of values of Θ taken in $[0, \frac{\pi}{2}]$). If the integration with respect to the variable Φ is performed analytically (as is the case in (64a)), the degree of accuracy of the sets $\mathcal{S}'_{21}$ and $\mathcal{S}'_{120}$, in this preliminary analysis, is almost equal to the one obtained with $m = 21$ and $m = 120$ equidistributed points, respectively, whereas the outcomes of the new set $\mathcal{I} \times \mathcal{J}$ is less accurate than the one obtainable with the same number of equidistributed points. The coloured squares represent, respectively, the errors err_{int} computed by employing $\mathcal{I} \times \mathcal{J}$ (magenta), $\mathcal{S}'_{21}$ (orange), and $\mathcal{S}'_{120}$ (green), for $\hat{\Psi} = \hat{\Psi}_2$. Differently from the case of the pseudo-Gaussian distribution, the magenta square representing err_{int} for the new set $\mathcal{I} \times \mathcal{J}$ lies under the blue, squared curve obtained for the case of equidistributed points, thereby producing a better result in the evaluation of $(\boldsymbol{Z}_0)^{11}$. Concerning $\mathcal{S}'_{21}$, we obtain a less accurate result than in the case of 21 equidistributed points, whereas the result obtained by employing $\mathcal{S}'_{120}$ is almost exact, as the corresponing value of the error is smaller than the one obtained with the same number of equidistributed points. We can notice that, for both the probability densities considered in the present study, the new set of points returns almost the same degree of accuracy, whereas the two considered sets of Sloane points ($\mathcal{S}'_{21}$ and $\mathcal{S}'_{120}$, respectively) are more influenced by the nature of the integrand.

Finally, we compare the computational time required for the algorithms A1 and A2. We see from Figure (6) that, by increasing the number of integration points, the SDA necessitates linearly increasing computational time, while the elapsed time for algorithm A2 increases almost linearly with the refinement of the grid vertices (which, at this stage, consist of the points needed to evaluate the depth dependent probability density distribution). We remark that the computational time reported in Figure 6 has been determined for a one-dimensional grid, represented by a given discrete set of values of the normalised axial coordinate ξ. Thus, it is not the overall time required for a full simulation. Indeed, in the full FEM model of (51a) and (51b), the routines shown in the algorithms A1 and A2 will be called for each point of the computational grid, and for each of the six independent components of $\boldsymbol{Z}$ and $\boldsymbol{S}_{\mathrm{a}}$. Thus, we may conclude from this first analysis that less, but properly chosen, integration points are preferable to an arbitrary big set of equidistributed points. The latter ones, however, lead to a solution that converges to the exact one, whereas the equispaced points do not, unless non-trivial weights are determined (see Figure 2). In the following, we present results of the routines A1 and A2. Afterwards, an *internal* implementation of the SDA is presented for the set of equidistributed points, for $\mathcal{S}'_{21}$ and $\mathcal{S}'_{120}$, and for the set of points proposed in $\mathcal{I} \times \mathcal{J}$. We will say that the implementation is *internal*, if no call to a Matlab routine is needed.

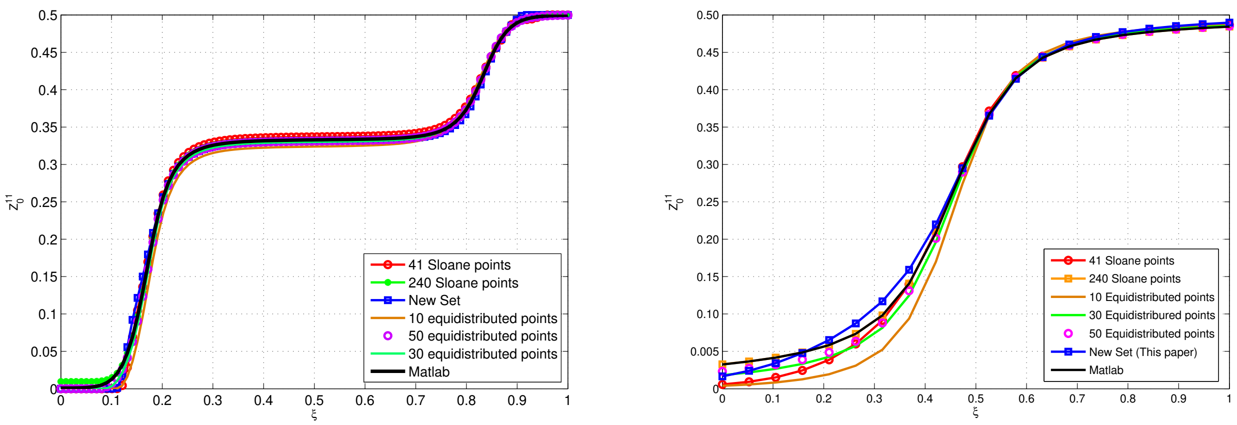

Fig. 4 Results of the evaluation of $(\boldsymbol{Z}_0)^{11}$ with different spherical designs. (a) Pseudo-Gaussian probability density distribution. (b) von Mises probability density distribution. The curves corresponding to the 41 and 240 Sloane points have been found by using, respectively, 21 and 120 points on the hemisphere $\mathbb{S}^{2+}_X\mathscr{B}$. All other sets of points refer to integrations on $\mathbb{S}^{2+}_X\mathscr{B}$.

Algorithm 1 –A1– SDA (Spherical Design Algortihm)

procedure SDA
  for $k = 1, \dots, M$ **do** *(M is the number of grid vertices)*
    Initialise $(\boldsymbol{S}_\mathrm{a})_k = \boldsymbol{0}$, $\boldsymbol{Z}_k = 0$, and $\mathcal{Z}_k = 0$ *(partial sums)*
    Load the point set $\{\mathcal{X}_{ij} \in \mathscr{D}\}_{i,j=1}^{N=mn}$ *(chosen in a proper way)*
    Load $Q(\xi_k)$ and $\sigma(\xi_k)$
    for $i = 1, \dots, m$ **do** *(inner cycle to evaluate the normalisation factor)*
      Evaluate $\hat{\gamma}_1(\xi_k, \Theta_i) = \exp\left(\frac{-(\Theta_i - Q(\xi_k))^2}{2[\sigma(\xi_k)]^2}\right)$
      $(\mathcal{Z}_1)_k = (\mathcal{Z}_1)_k + \frac{2\pi}{N}\hat{\gamma}_1(\xi_k, \Theta_i)$
    end for
    Calculate

$$(\hat{\Psi}_1)_{ik} = \hat{\Psi}_1(\xi_k, \Theta_i) = \frac{\hat{\gamma}_1(\xi_k, \Theta_i)}{(\mathcal{Z}_1)_k},\ i = 1, \dots, m$$

    Given $\boldsymbol{C}_k$ at time t:
    for $i = 1, \dots, m$ **do**
      for $j = 1, \dots, n$ **do**
        Evaluate $(I_4)_{ijk} = \mathrm{tr}(\boldsymbol{C}_k \boldsymbol{A}_{ij})$, and
        $\boldsymbol{A}_{ij} = \boldsymbol{M}_{ij} \otimes \boldsymbol{M}_{ij}$, with $\boldsymbol{M}_{ij} = \hat{\boldsymbol{M}}(\Theta_i, \Phi_j)$
        if $(\hat{\Psi}_1)_{ik} > \mathrm{tol}_{(\Psi)}$ **then**
          $(\boldsymbol{Z}_\mathrm{par})_{ijk} = (\hat{\Psi}_1)_{ik} \frac{\boldsymbol{A}_{ij}}{(I_4)_{ijk}}$
          $\boldsymbol{Z}_k = \boldsymbol{Z}_k + \frac{2\pi}{N}(\boldsymbol{Z}_\mathrm{par})_{ijk}$ *(Partial sum has to be uploaded)*
          if $(I_4)_{ijk} > 1$ **then**
            $(\boldsymbol{S}^{(0)}_\mathrm{par})_{ijk} = (\hat{\Psi}_1)_{ik}[(I_4)_{ijk} - 1]\boldsymbol{A}_{ij}$
            $(\boldsymbol{S}_\mathrm{par})_{ijk} = 2\phi_{1\mathrm{sR}}c\,(\boldsymbol{S}^{(0)}_\mathrm{par})_{ijk}$
            $(\boldsymbol{S}_\mathrm{a})_k = (\boldsymbol{S}_\mathrm{a})_k + \frac{2\pi}{N}(\boldsymbol{S}_\mathrm{par})_{ijk}$ *(Partial sum has to be uploaded)*
          end if
        end if
      end for
    end for
  end for
end procedure

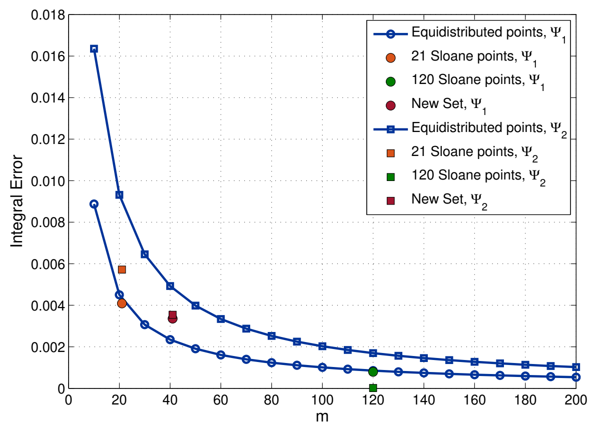

Fig. 5 Discrepancy err_int (see equation (66)), expressed as a function of the increasing number of equidistributed values of Θ_i, between the values of $(\boldsymbol{Z}_0)^{11}$ corresponding to the Matlab integration and the values of $(\boldsymbol{Z}_0)^{11}$ corresponding to a set of equidistributed points. The green, yellow, and magenta dots and squares correspond to the discrepancy obtained between the Matlab and the SDA outcomes for 21 and 120 Sloane points, and for the new set $\mathcal{I} \times \mathcal{J}$, respectively.

Algorithm 2 –A2– Matlab Integration Algorithm

procedure MATLAB INTEGRATION ALGORITHM (needs the call to the functions in algorithm (A3))
  for $k = 1, \dots M$ **do** *(M is the number of grid vertices)*
    $\mathcal{Z}_k = \mathrm{Integral}(@(\Theta)\hat{\gamma}_1(\Theta, \xi_k), 0, \pi)$
    Calculate $\hat{\Psi}_1(\Theta, \xi_k) = \frac{1}{(\mathcal{Z}_1)_k}\hat{\gamma}_1(\Theta, \xi_k)$.
    if $\hat{\Psi}_1(\Theta, \xi_k) > \mathrm{tol}_{(\Psi)}$ **then**
  $\boldsymbol{Z}_k = \mathrm{Integral2}(@(\Theta, \Phi)\boldsymbol{Z}_\mathrm{par}(\boldsymbol{C}_k, \Theta, \Phi), 0, \frac{\pi}{2}, 0, 2\pi)$
  $(\boldsymbol{S}_\mathrm{a})_k = \mathrm{Integral2}(@(\Theta, \Phi)\boldsymbol{S}_\mathrm{par}(\boldsymbol{C}_k, \Theta, \Phi), 0, \frac{\pi}{2}, 0, 2\pi)$
    end if
  end for
end procedure
(Note that, here, we employ the standard Matlab notation. In particular, the symbol @ represents the function handle constructor.)

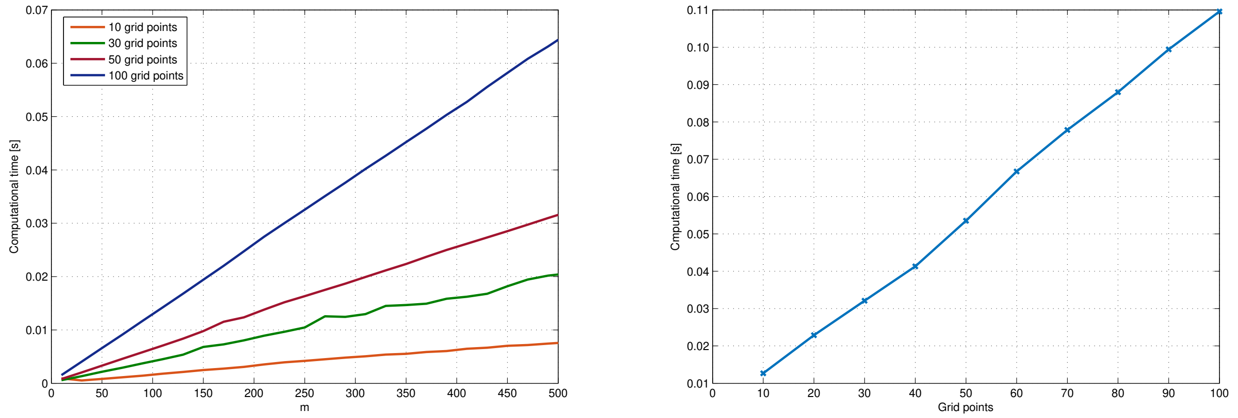

Fig. 6 Required computational time for the SDA algorithm (a) and for the algorithm A2 (b).

Algorithm 3 –A3– Functions for the Matlab Integration

---

procedure PROBABILITY DENSITY
  Load $Q(\xi_k)$ and $\sigma(\xi_k)$
  Set $\hat{\gamma}_1(\Theta,\xi_k) = \exp\left(\frac{-(\Theta - Q(\xi_k))^2}{2[\sigma(\xi_k)]^2}\right)$
end procedure

---

procedure HYDRAULIC CONDUCTIVITY
  Evaluate $I_4(\boldsymbol{C}_k, \boldsymbol{M}) = \hat{I}_4(\boldsymbol{C}_k, \Theta, \Phi)$, $\hat{\boldsymbol{A}}(\Theta, \Phi)$
  Set $\boldsymbol{Z}_{\text{par}}(\boldsymbol{C}_k, \Theta, \Phi) = \hat{\Psi}_1(\Theta, \xi_k) \frac{\hat{\boldsymbol{A}}(\Theta,\Phi)}{\hat{I}_4(\boldsymbol{C}_k,\Theta,\Phi)}$
end procedure

---

procedure STRESS
  Evaluate $\hat{I}_4(\boldsymbol{C}_k, \Theta, \Phi)$, $\hat{\boldsymbol{A}}(\Theta, \Phi)$
  if $(\hat{I}_4)_k := \hat{I}_4(\boldsymbol{C}_k, \Theta, \Phi) > 1$ **then**

$$\boldsymbol{S}_{\text{par}}(\boldsymbol{C}_k, \Theta, \Phi)[(\hat{I}_4)_k > 1] = 2\phi_{1\text{sR}} c \hat{\Psi}_1(\xi_k, \Theta)(\hat{I}_4(\boldsymbol{C}_k, \Theta, \Phi) - 1)\hat{\boldsymbol{A}}(\Theta, \Phi)[(\hat{I}_4)_k > 1]$$

  end if
(the "If" condition on the fourth invariant should be considered in the function that evaluates $\boldsymbol{S}_{\text{par}}$. The present code returns a tensor $\boldsymbol{S}_{\text{par}}$ whose components for which $(\hat{I}_4)_k \le 1$ are set equal to zero by means of the term $[(\hat{I}_4)_k > 1]$ in square brackets)
end procedure

---

5 Solution of a benchmark test

5.1 The unconfined compression test

Equations (51a) and (51b) are now solved for a specific benchmark test, along with appropriate boundary and initial conditions, and the constitutive functions defined in (45)–(49). In the inhomogeneous model of articular cartilage considered hereafter, these depend on material points through the volumetric fractions $\phi_{0\text{sR}}$ and $\phi_{1\text{sR}}$, and the referential permeability $k_{0\text{R}}$, which are assumed to vary with the normalised axial coordinate ξ as [58]

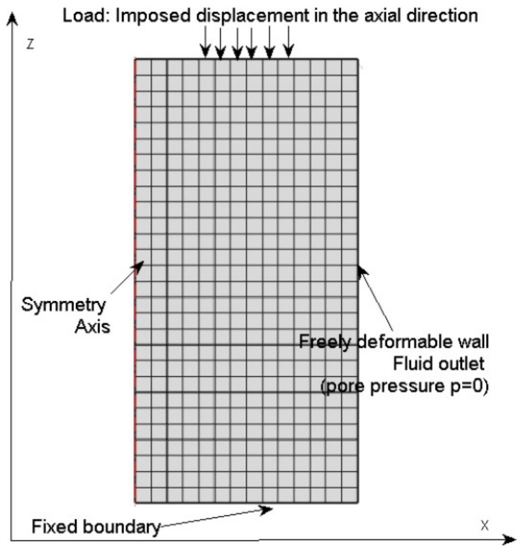

Fig. 7 Computational grid and boundary conditions of the unconfined compression benchmark.

$$\phi_{0\text{sR}}(\xi) = -0.062\xi^2 + 0.038\xi + 0.046, \tag{67a}$$

$$\phi_{1\text{sR}}(\xi) = +0.062\xi^2 - 0.138\xi + 0.404, \tag{67b}$$

$$\frac{k_{0\text{R}}(\xi)}{k_{0\text{R,hom}}} = \left(\frac{e_{\text{R}}(\xi)}{e_{\text{R,hom}}}\right)^{\kappa} \mathrm{e}^{\left(\frac{M}{2}\left[\left(\frac{1+e_{\text{R}}(\xi)}{1+e_{\text{R,hom}}}\right)^2 - 1\right]\right)}, \tag{67c}$$

where $e_{\text{R}} := (1 - \phi_{\text{sR}})/\phi_{\text{sR}}$, with $\phi_{\text{sR}} = \phi_{0\text{sR}} + \phi_{1\text{sR}}$, is referred to as "referential void ratio" (i.e., the ratio between the referential volumetric fraction of the voids, $1 - \phi_{\text{sR}}$, and the referential volumetric fraction of the solid phase as a whole, ϕ_{sR}), and $e_{\text{R,hom}}$ is a homogeneous value of the void ratio, taken as reference for the simulations. All the model parameters have been defined in Table 1.

The simulated benchmark problem is an unconfined compression test, performed on a cylindric sample of

Table 1 Constant values in the considered benchmark.

Name	Description	Value
μ_0	Matrix Shear Modulus	0.2716 [MPa]
μ_1	Fibres Shear Modulus	7.2727 [MPa]
λ_0	Matrix First Lamé's Constant	0.0556 [MPa]
λ_1	Fibres First Lamé's Constant	2.4828 [MPa]
c	Material Parameter in $\hat{W}_{1\mathrm{a}}(\boldsymbol{C})$	7.5062 [MPa]
$k_{0\mathrm{R,hom}}$	Reference scalar hydraulic conductivity	$3 \cdot 10^{-15}$ [m^4/(Ns)]
κ	Material parameter in (67c)	0.0848
M	Material parameter in (67c)	4.638
$e_{\mathrm{R,hom}}$	Homogeneous void ratio	4
R_0	Radius of the cylinder	0.5 [mm]
L	Height of the cylinder	1.0 [mm]
tol_{Ψ}	Tolerance on the probability density	$5 \cdot 10^{-5}$

articular cartilage of height L and circular cross section of radius R_0 in the undeformed configuration $\mathscr{B}$. The specimen is put between two parallel, impermeable plates, which are kept in contact with its top and bottom surfaces. During compression, the interstitial fluid flows out of the specimen through its lateral wall. The lower plate is held fixed and, in this work, the specimen is assumed to be clamped at this end in order to simulate the attachment of the tissue to the subchondral bone. The upper plate is moved axially either in force or in displacement control to mimic the load that the tissue has to bear in physiological or pathological conditions (for testing purposes, the experimental protocol sometimes imposes loading conditions far beyond the physiological range). In this work, a linearly increasing axial displacement w is applied to the upper plate by means of a loading ramp ending at 20% compression of the sample after $T = 20$ s, i.e.,

$$w(t) = -0.2L\frac{t}{T}. \tag{68}$$

In formulae, the boundary conditions describing the simulated experimental setting are given by:

$$\chi^3 = L + w, \qquad \boldsymbol{Q}.\boldsymbol{E}_3 = 0, \qquad \forall\, X \in \Gamma_{\mathrm{u}}, \tag{69a}$$

$$-\,p = 0, \qquad \boldsymbol{P}.\boldsymbol{N} = \boldsymbol{0}, \qquad \forall\, X \in \Gamma_{\mathrm{w}}, \tag{69b}$$

$$\chi(X,t) - \chi(X,0) = \boldsymbol{0}, \quad \boldsymbol{Q}.(-\boldsymbol{E}_3) = 0, \quad \forall\, X \in \Gamma_{\mathrm{l}}, \tag{69c}$$

where Γ_{u}, Γ_{l}, and Γ_{w} denote the upper, lower and lateral boundaries of the specimen, respectively, and the conditions (69a)–(69c) are intended to apply at all times $t \in [0, T]$. The unit vectors $\boldsymbol{N}$ and $\boldsymbol{E}_3$ represent the radial and axial directions of the sample, respectively. Usually, the height of the tissue at the end of the loading ramp, i.e., $L_T = L + w(T) = 0.8L$ ($w(T) \le 0$), is maintained constant over a given time interval, during which the fluid filtration velocity and the pore pressure relax, while the constitutive part of the stress reaches a constant value that depends on the degree of compression to be maintained. Since in this work we are interested in the numerical performances of the SDA, and not in the way in which the system relaxes towards its stationary state, we present simulations referred to the loading ramp only.

5.2 The Finite Element setting

A schematic representation of the chosen mesh, and the above described boundary conditions are reported in Figure 7. Equations (51a) and (51b) were solved numerically, along with the boundary conditions (69a)–(69c) and the initial condition $J(X, 0) = 1$, by means of a damped Newton method and a Backward Differentiation Formula (BDF) for the time discretisation. The BDF is a multi-step generalisation of the Backward Euler scheme. It is characterised by an integer number s, normally ranging between 1 and 6, and thereby determining the order of the scheme (for further details, the Reader is referred to [1,40]). When $s = 1$, the BDF coincides with the Backward Euler method. In our simulations, s ranges between 1 and 5, and the damping coefficient used in the Newton method is automatically chosen by the solvers of our commercial software.

In the remainder of this section, we describe how the quadrature method used to determine the directional averages couples with the FE implementation of the model equations. To this end, we sketch the time and space discretisation of the functionals (51a) and (51b). This is, in fact, an extension of the discretisation presented in [27,31] to the case of anisotropic, biphasic media. Notice that, from here on, the quantities with a superimposed tilde pertain to the test functions associted with the sets defined in (52a) and (52b). Moreover, for any function f defined on $\mathscr{B} \times \mathscr{I}$, the notation

$f^j \equiv f(X, t^j)$ applies, for all j. With reference to (51a), in which the time-derivative of J features explicitly, we suppose for demonstrational purposes that the time discretisation reduces to a first order BDF, and we write

$$\dot{J} \approx \frac{J^j - J^{j-1}}{\tau_j}, \quad \tau_j = t_j - t_{j-1}, \quad j \geq 1,\ j \in \mathbb{N}, \quad (70)$$

with $\tau_j > 0$ being the width of the jth time step. At the jth time step, the time-discrete version of the functionals (51a) and (51b) takes on the form

$$0 = \mathfrak{F}^j_\chi = \int_{\mathscr{B}} \boldsymbol{P}^j : \boldsymbol{g}\,\mathrm{Grad}\,\tilde{\boldsymbol{u}}, \quad (71)$$

$$0 = \mathfrak{F}^j_p = -\int_{\mathscr{B}} (\mathrm{Grad}\,\tilde{p})\boldsymbol{K}^j(\mathrm{Grad}\,p^j) - \int_{\mathscr{B}} \tilde{p}\frac{J^j - J^{j-1}}{\tau^j}, \quad (72)$$

with $\boldsymbol{P}^j \equiv \hat{\boldsymbol{P}}(p^j, \boldsymbol{F}^j)$, and $\boldsymbol{K}^j \equiv \hat{\boldsymbol{K}}(\boldsymbol{F}^j)$. Next, we consider the overall first Piola-Kirchhoff stress tensor, $\hat{\boldsymbol{P}}(p, \boldsymbol{F})$, whose expression we rearrange as

$$\hat{\boldsymbol{P}}(p, \boldsymbol{F}) = -Jp\boldsymbol{g}^{-1}\boldsymbol{F}^{-\mathrm{T}} + \hat{\boldsymbol{P}}_0(\boldsymbol{F}) + \hat{\boldsymbol{P}}_\mathrm{a}(\boldsymbol{F}), \quad (73)$$

with

$$\hat{\boldsymbol{P}}_0(\boldsymbol{F}) = \lambda \ln(J)\boldsymbol{g}^{-1}\boldsymbol{F}^{-\mathrm{T}} + \mu\boldsymbol{F}\left(\boldsymbol{G}^{-1} - \boldsymbol{C}^{-1}\right), \quad (74)$$

$$\hat{\boldsymbol{P}}_\mathrm{a}(\boldsymbol{F}) = \boldsymbol{F}\hat{\boldsymbol{S}}_\mathrm{a}(\boldsymbol{C}), \quad (75)$$

and $\hat{\boldsymbol{S}}_\mathrm{a}(\boldsymbol{C})$ being defined in (46). Analogously, by invoking the expression of the material permeability in (47), we split $\hat{\boldsymbol{K}}(\boldsymbol{F})$ as

$$\hat{\boldsymbol{K}}(\boldsymbol{F}) = \hat{\boldsymbol{K}}_0(\boldsymbol{F}) + \hat{\kappa}(\boldsymbol{F})\hat{\boldsymbol{Z}}(\boldsymbol{C}), \quad (76)$$

where we have set

$$\hat{\boldsymbol{K}}_0(\boldsymbol{F}) = \hat{k}_0(J)\frac{(J - \phi_{1\mathrm{sR}})^2}{J}\boldsymbol{C}^{-1}, \quad (77a)$$

$$\hat{\kappa}(\boldsymbol{F}) = \hat{k}_0(J)\frac{(J - \phi_{1\mathrm{sR}})\phi_{1\mathrm{sR}}}{J}, \quad J = \det(\boldsymbol{F}). \quad (77b)$$

The decompositions (73) and (76) are done in order to highlight the presence of the anisotropic summands, $\hat{\boldsymbol{P}}_\mathrm{a}(\boldsymbol{F})$ and $\hat{\kappa}(\boldsymbol{F})\hat{\boldsymbol{Z}}(\boldsymbol{C})$, and their implementation in the Finite Element method. Indeed, by accounting for (73) and (76), the time-discrete version of the functionals $\mathfrak{F}_\chi$ and $\mathfrak{F}_p$ at the instant of time t_j reads

$$0 = \mathfrak{F}^j_\chi = \int_{\mathscr{B}} \left\{-J^j p^j \boldsymbol{g}^{-1}(\boldsymbol{F}^j)^{-\mathrm{T}} : \boldsymbol{g}\tilde{\boldsymbol{H}}\right\} + \int_{\mathscr{B}} \boldsymbol{P}^j_0 : \boldsymbol{g}\tilde{\boldsymbol{H}} + \int_{\mathscr{B}} \boldsymbol{F}^j\boldsymbol{S}^j_\mathrm{a} : \boldsymbol{g}\tilde{\boldsymbol{H}}, \quad (78a)$$

$$0 = \mathfrak{F}^j_p = -\int_{\mathscr{B}} (\mathrm{Grad}\,\tilde{p})\boldsymbol{K}^j_0(\mathrm{Grad}\,p^j) - \int_{\mathscr{B}} (\mathrm{Grad}\,\tilde{p})\kappa^j\boldsymbol{Z}^j(\mathrm{Grad}\,p^j) - \int_{\mathscr{B}} \tilde{p}\frac{J^j - J^{j-1}}{\tau^j}, \quad (78b)$$

in which $\tilde{\boldsymbol{H}} \equiv \mathrm{Grad}\,\tilde{\boldsymbol{u}}$, and $\boldsymbol{P}^j_0 \equiv \hat{\boldsymbol{P}}_0(\boldsymbol{F}^j)$, $\boldsymbol{K}^j_0 = \hat{\boldsymbol{K}}_0(\boldsymbol{F}^j)$, $\kappa^j = \hat{\kappa}(\boldsymbol{F}^j)$, and

$$\boldsymbol{S}^j_\mathrm{a} \equiv \hat{\boldsymbol{S}}_\mathrm{a}(\boldsymbol{C}^j) = 2\phi_{1\mathrm{sR}}c\int_{\mathbb{S}^{2+}_X\mathscr{B}} \varPsi(\boldsymbol{M})\mathcal{H}(I^j_4 - 1)[I^j_4 - 1]\boldsymbol{A}, \quad (79a)$$

$$\boldsymbol{Z}^j \equiv \hat{\boldsymbol{Z}}(\boldsymbol{C}^j) = \int_{\mathbb{S}^{2+}_X\mathscr{B}} \varPsi(\boldsymbol{M})\frac{\boldsymbol{M}\otimes\boldsymbol{M}}{I^j_4}. \quad (79b)$$

It should be noticed that, because of the integral over $\mathbb{S}^{2+}_X\mathscr{B}$ in (79a) and (79b), the third summand on the right-hand-side of (78a) and the second summand on the right-hand-side of (78b) feature two integrations, which have to be performed hierarchically: First, one has to solve at each time step the integral over $\mathbb{S}^{2+}_X\mathscr{B}$, and then the integral over $\mathscr{B}$. Since the problem is nonlinear, we look for solutions by invoking Newton method. Hence, at the jth time step, and within the kth Newton iteration ($k \geq 1$, $k \in \mathbb{N}$), we solve the linearised equations

$$\mathfrak{F}^{j,k-1}_\chi + \mathfrak{D}_\chi\mathfrak{F}^{j,k-1}_\chi[\boldsymbol{h}^{j,k}] + \mathfrak{D}_p\mathfrak{F}^{j,k-1}_\chi[\vartheta^{j,k}] = 0, \quad (80a)$$

$$\mathfrak{F}^{j,k-1}_p + \mathfrak{D}_\chi\mathfrak{F}^{j,k-1}_p[\boldsymbol{h}^{j,k}] + \mathfrak{D}_p\mathfrak{F}^{j,k-1}_p[\vartheta^{j,k}] = 0, \quad (80b)$$

in which we adopted the notation

$$\mathfrak{F}^{j,k-1}_\chi = \mathfrak{F}_\chi(\chi^{j,k-1}, p^{j,k-1}), \quad (81a)$$

$$\mathfrak{F}^{j,k-1}_p = \mathfrak{F}_p(\chi^{j,k-1}, p^{j,k-1}), \quad (81b)$$

$\mathfrak{D}_\chi$ and $\mathfrak{D}_p$ indicate Gâteaux differentiation with respect to χ and p, respectively, and $\boldsymbol{h}^{j,k}$ and $\vartheta^{j,k}$ are the incremements associated with the motion and the pressure, respectively, along which the Gâteaux derivatives are computed, i.e.,

$$\chi^{j,k} = \chi^{j,k-1} + \boldsymbol{h}^{j,k}, \quad (82a)$$

$$p^{j,k} = p^{j,k-1} + \vartheta^{j,k}. \quad (82b)$$

The explicit computation of the Gâteaux derivatives in (80a) and (80b) trasforms the linearised variational problem (78a)–(78b) into the abstract form [31]

$$A(\boldsymbol{h}^{j,k}, \tilde{\boldsymbol{u}}) - B(\vartheta^{j,k}, \tilde{\boldsymbol{u}}) = -\mathfrak{F}^{j,k-1}_\chi, \quad \forall\, \tilde{\boldsymbol{u}} \in \tilde{\mathscr{V}}, \quad (83a)$$

$$-C(\boldsymbol{h}^{j,k}, \tilde{p}) - D(\vartheta^{j,k}, \tilde{p}) = -\mathfrak{F}^{j,k-1}_p, \quad \forall\, \tilde{p} \in \tilde{\mathscr{P}}, \quad (83b)$$

which should be solved for the increments $\boldsymbol{h}^{j,k}$ and $\theta^{j,k}$. In (83a) and (83b) we define the bilinear forms [31]

$$\begin{aligned}
A(\boldsymbol{h}^{j,k}, \tilde{\boldsymbol{u}}) &= \mathfrak{D}_\chi \mathfrak{F}_\chi^{j,k-1}[\boldsymbol{h}^{j,k}] \\
&= \int_{\mathscr{B}} \boldsymbol{g}\tilde{\boldsymbol{H}} : \mathbb{A}^{j,k-1} : \boldsymbol{H}^{j,k}, && \text{(84a)} \\
-B(\vartheta^{j,k}, \tilde{\boldsymbol{u}}) &= \mathfrak{D}_p \mathfrak{F}_\chi^{j,k-1}[\vartheta^{j,k}] \\
&= \int_{\mathscr{B}} \left\{ -J^{j,k-1}\vartheta^{j,k} \boldsymbol{g}^{-1} (\boldsymbol{F}^{j,k-1})^{-\mathrm{T}} : \boldsymbol{g}\tilde{\boldsymbol{H}} \right\}, && \text{(84b)} \\
-C(\boldsymbol{h}^{j,k}, \tilde{p}) &= \mathfrak{D}_\chi \mathfrak{F}_p^{j,k-1}[\boldsymbol{h}^{j,k}] \\
&= -\frac{B(\boldsymbol{h}^{j,k}, \tilde{p})}{\tau_j} \\
&\quad - \int_{\mathscr{B}} (\operatorname{Grad} \tilde{p}) \Big(\mathbb{K}^{j,k-1} : \boldsymbol{H}^{j,k} \Big) (\operatorname{Grad} p^{j,k-1}), && \text{(84c)} \\
-D(\vartheta^{j,k}, \tilde{p}) &= \mathfrak{D}_p \mathfrak{F}_p^{j,k-1}[\vartheta^{j,k}] \\
&= -\int_{\mathscr{B}} (\operatorname{Grad} \tilde{p}) \boldsymbol{K}^{j,k-1} (\operatorname{Grad} \vartheta^{j,k}), && \text{(84d)}
\end{aligned}$$

where $\boldsymbol{H}^{j,k} = \operatorname{Grad} \boldsymbol{h}^{j,k}$, $\mathbb{A}^{j,k-1}$ is the algorithmic first elasticity tensor [47], and $\mathbb{K}^{j,k-1}$ in (84c) is given by

$$\mathbb{K}^{j,k-1} \equiv \frac{\partial \hat{\boldsymbol{K}}}{\partial \boldsymbol{F}} (\boldsymbol{F}^{j,k-1}). \tag{85}$$

The SDA (or the Matlab integration) comes into play in the computation of $\mathbb{A}^{j,k-1}$, $\boldsymbol{K}^{j,k-1}$, and $\mathbb{K}^{j,k-1}$. Let us consider, for instance, the expression of the elasticity tensor, and let us split it into a "standard", isotropic part, $\mathbb{A}_{\mathrm{st}}^{j,k-1}$, and a "non-standard", anisotropic part pertaining to the fibres, $\mathbb{A}_{\mathrm{e}}^{j,k-1}$, i.e.,

$$\begin{aligned}
\mathbb{A}^{j,k-1} &= \mathbb{A}_{\mathrm{st}}^{j,k-1} + \frac{\partial \hat{\boldsymbol{P}}_{\mathrm{a}}}{\partial \boldsymbol{F}} (\boldsymbol{F}^{j,k-1}) \\
&= \mathbb{A}_{\mathrm{st}}^{j,k-1} + \mathbb{A}_{\mathrm{e}}^{j,k-1}.
\end{aligned} \tag{86}$$

The standard elasticity tensor $\mathbb{A}_{\mathrm{st}}^{j,k-1}$ contains all the terms stemming from the incompressibility constraint, the energetic contribution of the penalty term (40), and the terms pertaining to the isotropic part of the model, whereas the non standard contribution is such that the following identity holds

$$\begin{aligned}
\boldsymbol{g}\tilde{\boldsymbol{H}} : \mathbb{A}_{\mathrm{e}}^{j,k-1} : \boldsymbol{H}^{j,k} &= \operatorname{sym}(\tilde{\boldsymbol{H}}^{\mathrm{T}} . \boldsymbol{H}^{j,k}) : \boldsymbol{S}_{\mathrm{a}}^{j,k-1} \\
&\quad + [(\boldsymbol{F}^{j,k-1})^{\mathrm{T}} . \tilde{\boldsymbol{H}}] : \mathbb{C}_{\mathrm{e}}^{j,k-1} : [(\boldsymbol{F}^{j,k-1})^{\mathrm{T}} . \boldsymbol{H}^{j,k}],
\end{aligned} \tag{87}$$

where $\boldsymbol{S}_{\mathrm{a}}^{j,k-1}$ is obtained from (79a) by substituting I_4^j with the value of the invariant at the $(k-1)$th Newton iteration, i.e., with $I_4^{j,k-1}$, and

$$\mathbb{C}_{\mathrm{e}}^{j,k-1} = 4\phi_{1\mathrm{sR}} c \int_{\mathbb{S}_X^{2+}\mathscr{B}} \Psi(\boldsymbol{M}) \mathcal{H}(I_4^{j,k-1} - 1) \boldsymbol{A} \otimes \boldsymbol{A}. \tag{88}$$

Analogously, $\boldsymbol{K}^{j,k-1} = \hat{\boldsymbol{K}}(\boldsymbol{F}^{j,k-1})$ splits as follows

$$\boldsymbol{K}^{j,k-1} = \boldsymbol{K}_0^{j,k-1} + \kappa^{j,k-1} \boldsymbol{Z}^{j,k-1}, \tag{89}$$

where

$$\kappa^{j,k-1} \equiv \hat{k}_0(J^{j,k-1}) \frac{(J^{j,k-1} - \phi_{1\mathrm{sR}})\phi_{1\mathrm{sR}}}{J^{j,k-1}}, \tag{90a}$$

$$\boldsymbol{K}_0^{j,k-1} = \hat{k}_0(J^{j,k-1}) \frac{(J^{j,k-1} - \phi_{1\mathrm{sR}})^2}{J^{j,k-1}} (\boldsymbol{C}^{j,k-1})^{-1}, \tag{90b}$$

$$\boldsymbol{Z}^{j,k-1} = \int_{\mathbb{S}_X^{2+}\mathscr{B}} \Psi(\boldsymbol{M}) \frac{\boldsymbol{M} \otimes \boldsymbol{M}}{I_4^{j,k-1}}, \tag{90c}$$

and $\mathbb{K}^{j,k-1}$ is such that

$$\begin{aligned}
\mathbb{K}^{j,k-1} : \boldsymbol{H}^{j,k} = &\mathbb{K}_0^{j,k-1} : \boldsymbol{H}^{j,k} \\
&+ \left[\frac{\partial \hat{\kappa}}{\partial \boldsymbol{F}} (\boldsymbol{F}^{j,k-1}) : \boldsymbol{H}^{j,k} \right] \boldsymbol{Z}^{j,k-1} \\
&+ \kappa^{j,k-1} \left[\frac{\partial \hat{\boldsymbol{Z}}}{\partial \boldsymbol{F}} (\boldsymbol{F}^{j,k-1}) : \boldsymbol{H}^{j,k} \right],
\end{aligned} \tag{91}$$

with

$$\mathbb{K}_0^{j,k-1} = \frac{\partial \hat{\boldsymbol{K}}_0}{\partial \boldsymbol{F}} (\boldsymbol{F}^{j,k-1}). \tag{92}$$

Note, in particular, that the term between brackets in the third summand on the right-hand-side of (91) is given by

$$\begin{aligned}
&\left[\frac{\partial \hat{\boldsymbol{Z}}}{\partial \boldsymbol{F}} (\boldsymbol{F}^{j,k-1}) : \boldsymbol{H}^{j,k} \right] \\
&= -2 \int_{\mathbb{S}_X^{2+}\mathscr{B}} \Psi(\boldsymbol{M}) \frac{\boldsymbol{A}}{(I_4^{j,k-1})^2} \left[\boldsymbol{A} : \Big((\boldsymbol{F}^{j,k-1})^{\mathrm{T}} . \boldsymbol{H}^{j,k} \Big) \right],
\end{aligned} \tag{93}$$

with $\boldsymbol{A} = \boldsymbol{M} \otimes \boldsymbol{M}$ and $I_4^{j,k-1} = \boldsymbol{A} : \boldsymbol{C}^{j,k-1}$. The integral in (93) is nontrivial due to the presence of highly oscillating functions, which manifest themselves when polar coordinates are used.

Both the SDA and the Matlab integration come into play at each time step and within each Newton iteration performed to construct $A(\boldsymbol{h}^{j,k}, \tilde{\boldsymbol{u}})$, $C(\boldsymbol{h}^{j,k}, \tilde{p})$, and $D(\vartheta^{j,k}, \tilde{p})$ (cf. (84a), (84c), and (84d)). In particular, they are adopted to compute the integrals over $\mathbb{S}_X^{2+}\mathscr{B}$ that appear in the evaluation of $\boldsymbol{S}_{\mathrm{a}}^{j,k-1}$, $\mathbb{C}_{\mathrm{e}}^{j,k-1}$, $\boldsymbol{Z}^{j,k-1}$, and $\partial_{\boldsymbol{F}} \hat{\boldsymbol{Z}}(\boldsymbol{F}^{j,k-1})$. For this purpose, the quadrature methods are invoked at each integration point of each grid element, during the assembly of the "stiffness matrix". The computational effort of this procedure is related to the number of integration points within each element of the FE discretisation. Thus, if, for instance (in a 2D mesh), each element features 4 integration points, then 4×(number of elements) calls to the algorithms A1 (or A2) per time step and per linearisation iteration are required.

It is worthwhile to mention that the basis functions of the Finite Element discretisation are necessary to determine $\boldsymbol{S}_{\mathrm{a}}^{j,k-1}$, $\mathbb{C}_{\mathrm{e}}^{j,k-1}$, $\boldsymbol{Z}^{j,k-1}$, and $\partial_{\boldsymbol{F}} \hat{\boldsymbol{Z}}(\boldsymbol{F}^{j,k-1})$.

This occurs because each of these quantities depends on $I_4^{j,k-1}$, which, in turn, requires the interpolation of $\boldsymbol{C}^{j,k-1} = (\boldsymbol{F}^{j,k-1})^{\mathrm{T}}\boldsymbol{g}\boldsymbol{F}^{j,k-1}$ and, thus, of $\boldsymbol{F}^{j,k-1}$. To highlight the relation between the basis functions and $I_4^{j,k-1}$, let us first introduce the grid function ${}^h\chi$ approximating the motion at the jth instant of time and at the $(k-1)$th Newton iteration:

$$({}^h\chi^a)^{j,k-1} = \sum_{i=1}^{\mathscr{N}} (\chi^{a(i)})^{j,k-1}\varphi_{(i)}, \tag{94}$$

where $\{\varphi_{(i)}\}_{i=1}^{\mathscr{N}}$ is the set of basis functions, and $\mathscr{N}$ is the number of nodes. Consequently, the generic components of the grid functions ${}^h\boldsymbol{F}^{j,k-1}$ and ${}^h\boldsymbol{C}^{j,k-1}$ are given by

$$({}^hF^a{}_A)^{j,k-1} = \sum_{i=1}^{\mathscr{N}} (\chi^{a(i)})^{j,k-1}\frac{\partial\varphi_{(i)}}{\partial X^A}, \tag{95a}$$

$$({}^hC_{BD})^{j,k-1} = g_{ab}({}^hF^a{}_B)^{j,k-1}({}^hF^b{}_D)^{j,k-1}, \tag{95b}$$

which implies that $I_4^{j,k-1}$ is approximated by the grid function

$$\begin{aligned}({}^hI_4)^{j,k-1} &= ({}^hC_{BD})^{j,k-1}A^{BD}\\ &= g_{ab}\sum_{i,l=1}^{\mathscr{N}} (\chi^{a(i)})^{j,k-1}(\chi^{b(l)})^{j,k-1}\frac{\partial\varphi_{(i)}}{\partial X^B}\frac{\partial\varphi_{(l)}}{\partial X^D}A^{BD}\end{aligned} \tag{96}$$

(note that in (95b) and (96) Einstein's convention on repeated indices is used to denote the summation over $a, b = 1, 2, 3$ and $A, B = 1, 2, 3$). It follows from (96) that $({}^hI_4)^{j,k-1}$ necessitates the derivatives of the basis functions, as well as the coefficients $(\chi^{a(i)})^{j,k-1}$. These are, in fact, the inputs that a quadrature scheme (be it the SDA or the Matlab routine) receives from the FE discretisation at the $(k-1)$th Newton iteration within the jth time step.

In our simulations, polynomial basis functions of degree one, two, and three are tested. Due to the elementwise smoothness of the basis functions, the presence of their derivatives in (96) does not worsen in a significant way the integration procedure. However, varying the degree of the polynomials may yield to appreciably different performances, as we could see by running a FE simulation of a simplified, isotropic version of the model in which the fibres are absent (in this case, $\boldsymbol{K} = \boldsymbol{K}_0 = \hat{k}_0(J)J\boldsymbol{C}^{-1}$ and $\boldsymbol{S}_{\mathrm{a}} = \boldsymbol{0}$, so that neither the SDA nor the Matlab integration scheme are necessary). We found that quadratic Lagrangian polynomials are the optimal choice for discretising both the displacements and the pressure. Indeed, if linear basis functions are used, an oscillatory solution is obtained for some components of the stress and the permeability of the system.

Concerning the grid convergence of the mesh reported in Figure 7, we compared three different quadrangular meshes to a finer one (1250 elements).

In Table 2, the relative integral errors in the output curves representing the components of $\boldsymbol{Z}$, and those of $\boldsymbol{S}_{\mathrm{a}}$, are reported. To compute such errors, we applied the following formulae

$$\mathrm{err}_\xi = \frac{|\int_0^1 \mathcal{Q}_{\mathrm{i}}\mathrm{d}\xi - \int_0^1 \mathcal{Q}_{\mathrm{finer}}\mathrm{d}\xi|}{|\int_0^1 \mathcal{Q}_{\mathrm{finer}}\mathrm{d}\xi|}, \tag{97}$$

$$\mathrm{err}_t = \frac{|\int_0^{\mathrm{T}} \mathcal{Q}_{\mathrm{i}}\mathrm{d}t - \int_0^{\mathrm{T}} \mathcal{Q}_{\mathrm{finer}}\mathrm{d}t|}{|\int_0^{\mathrm{T}} \mathcal{Q}_{\mathrm{finer}}\mathrm{d}t|}, \tag{98}$$

where the index i denotes the type of mesh, i.e., i = Coarse, Intermediate, Fine, $\mathcal{Q}$ is one of the generic quantity of the model, and T represents the final instant of the loading ramp.

The pressure p, the norm of the displacement $\boldsymbol{u}$, and the von Mises equivalent stress σ_{VM}, to which Table 2 refers, are the results of a pointwise evaluation, in the point $X_1 = (0, 0, \frac{L}{2})$, for the pressure, and $X_2 = (\frac{R}{2}, \frac{R}{2}, \frac{L}{2})$, for the velocity and the stress. The components of the tensors $\boldsymbol{Z}$ and $\boldsymbol{S}_{\mathrm{a}}$ used to evaluate the errors are, instead, taken over the depth of the sample.

As visible from the reported errors, the discrepancy between the results obtained with progressively finer grids are small. Thus, with the grid represented in Figure 7 (fine grid of Table 2), we already reached the mesh convergence. Note that the integrations for computing the errors in (97) have been performed by means of a trapezoidal numerical integration.

As previously specified, the simulations were run by adopting two different methods for the solution of the integrals over $\mathbb{S}^{2+}_X\mathscr{B}$. The first method, outlined in A1, is the SDA, while the second method is the integration routine A2. For the SDA (either *internal* or in Matlab), at each $X \in \mathscr{B}$, an appropriate set of points was chosen on $\mathbb{S}^2_X\mathscr{B}$. The algorithm A2 is performed with fixed absolute and relative tolerances in the Matlab quadrature.

6 Results

6.1 Matlab validation

Before presenting the results of the inhomogeneous and transversely isotropic model of articular cartilage (see sections 2.1, 2.4, and 3.2), we show a second set of preliminary results to evaluate the performances of the routine A2 in the context of FEM simulations. This is done because the algorithm A2 is the basis for comparison

Table 2 Grid Convergence

	Coarse (50 elem.)	Intermediate (120 elem.)	Fine (392 elem.)
$\mathrm{err}_\xi(Z_0^{11}(t=0))$	$7.5 \cdot 10^{-7}$	$3.8 \cdot 10^{-7}$	$4.9 \cdot 10^{-8}$
$\mathrm{err}_\xi(Z_0^{11}(t=20))$	$5.8 \cdot 10^{-4}$	$4.4 \cdot 10^{-4}$	$3.9 \cdot 10^{-4}$
$\mathrm{err}_\xi(Z_0^{33}(t=0))$	$4.7 \cdot 10^{-7}$	$1.1 \cdot 10^{-7}$	$1.6 \cdot 10^{-8}$
$\mathrm{err}_\xi(Z_0^{33}(t=20))$	$2.7 \cdot 10^{-4}$	$8.7 \cdot 10^{-5}$	$4.4 \cdot 10^{-4}$
$\mathrm{err}_\xi((\boldsymbol{S}_\mathrm{a})^{11})$	$6.6 \cdot 10^{-3}$	$5.2 \cdot 10^{-3}$	$4.8 \cdot 10^{-3}$
$\mathrm{err}_\xi((\boldsymbol{S}_\mathrm{a})^{33})$	$4.5 \cdot 10^{-3}$	$4.5 \cdot 10^{-3}$	$5.5 \cdot 10^{-3}$
$\mathrm{err}_t(p)$	$6.2 \cdot 10^{-3}$	$3.8 \cdot 10^{-3}$	$3.0 \cdot 10^{-4}$
$\mathrm{err}_t(\|\boldsymbol{u}\|)$	$7.1 \cdot 10^{-4}$	$9.0 \cdot 10^{-4}$	$3.0 \cdot 10^{-4}$
$\mathrm{err}_t(\sigma_{VM})$	$2.2 \cdot 10^{-3}$	$1.1 \cdot 10^{-3}$	$3.0 \cdot 10^{-4}$

with the SDA. More specifically, it has been checked for no error propagation in time due to the coupling between the FEM solver and the routine A2. We remark that the Matlab routine "Integral" (cf. Algorithm A2) chooses the numerical quadrature method depending on the kind of function that has to be integrated. A control on the quality of the integration can be done by manipulating the absolute and the relative tolerances in the error associated with the quadrature results. Here, the considered default values for these tolerances, denoted in Matlab by AbsTol and RelTol, respectively, are AbsTol $= 1 \cdot 10^{-10}$ and RelTol $= 1 \cdot 10^{-6}$. In fact, although $(\boldsymbol{Z}_0)^{11}$ is decoupled from deformation, the integral in (64a) cannot be performed exactly.

For the purposes outlined above, we consider in this section the simple case of a homogeneous and isotropic material model, with the probability density (35b). In particular, we set $\phi_{0\mathrm{sR}} = 0.1$ and $\phi_{1\mathrm{sR}} = 0.3$ everywhere in the computational domain, and we assume that the probability density distribution reduces to $\hat{\Psi}_1(\xi, \Theta) = 1/2\pi$ for all values of $\xi \in [0,1]$ and for all $\Theta \in [0, \frac{\pi}{2}]$. This means that the normalisation factor is $\mathcal{Z}_{1+} = 2\pi \approx 6.2832$. Note that the values $\phi_{0\mathrm{sR}} = 0.1$ and $\phi_{1\mathrm{sR}} = 0.3$ are not taken from (67a) and (67b), and do not correspond to a value of $\xi \in [0,1]$.

Furthermore, in order to make the integral defining $\boldsymbol{Z}$ in (48) exactly solvable, we enforce the (strong) assumption that $\boldsymbol{Z}$, in a neighbourhood of $I_4(\boldsymbol{C}, \boldsymbol{M}) = 1$, reduces to

$$\boldsymbol{Z} = \int_{\mathbb{S}^{2+}_X \mathscr{B}} \Psi_1(\boldsymbol{M}) \frac{\boldsymbol{M} \otimes \boldsymbol{M}}{I_4(\boldsymbol{C}, \boldsymbol{M})} \approx \frac{1}{2\pi} \int_{\mathbb{S}^{2+}_X \mathscr{B}} \boldsymbol{M} \otimes \boldsymbol{M}. \tag{99}$$

Accordingly, the components of $\boldsymbol{Z}$ are given by

$$\boldsymbol{Z}^{12} = \boldsymbol{Z}^{13} = \boldsymbol{Z}^{23} = 0, \tag{100a}$$

$$\boldsymbol{Z}^{11} = \boldsymbol{Z}^{22} = \boldsymbol{Z}^{33} = Z, \tag{100b}$$

in which all the three diagonal components of $\boldsymbol{Z}$ are set equal to $Z = \frac{1}{3}$, the material being isotropic in this preliminary study. Finally, to solve exactly the integral in the definition (46) of $\boldsymbol{S}_\mathrm{a}$, we allow the fibres to contribute to the stress even when $I_4(\boldsymbol{C}, \boldsymbol{M})$ is smaller than unity. Note, however, that this simplification is sometimes physically sound in those situations in which the collagen fibres contribute to the overall compressive stiffness of cartilage [56]. In these cases, the Heaviside function can be eliminated from the expression of $\boldsymbol{S}_\mathrm{a}$, which becomes

$$\boldsymbol{S}_\mathrm{a} = \frac{2\phi_{1\mathrm{sR}} c}{2\pi} \int_{\mathbb{S}^{2+}_X \mathscr{B}} [I_4(\boldsymbol{C}, \boldsymbol{M}) - 1] \boldsymbol{M} \otimes \boldsymbol{M}. \tag{101}$$

Consequently, the diagonal components of $\boldsymbol{S}_\mathrm{a}$ are given by

$$(\boldsymbol{S}_\mathrm{a})^{11} = \frac{2\phi_{1\mathrm{sR}} c}{15} (3C_{11} + C_{22} + C_{33} - 5), \tag{102a}$$

$$(\boldsymbol{S}_\mathrm{a})^{22} = \frac{2\phi_{1\mathrm{sR}} c}{15} (C_{11} + 3C_{22} + C_{33} - 5), \tag{102b}$$

$$(\boldsymbol{S}_\mathrm{a})^{33} = \frac{2\phi_{1\mathrm{sR}} c}{15} (C_{11} + C_{22} + 3C_{33} - 5). \tag{102c}$$

We compare now the components of $\boldsymbol{Z}$ computed by means of the algorithm A2, Z_{A2}, with the components of $\boldsymbol{Z}$ determined in (100a) and (100b). We compute, thus, the mean relative deviation

$$\mathrm{Err}(Z) = \frac{Z_{\mathrm{A2}} - Z}{Z_{\mathrm{A2}}}, \tag{103}$$

which turns out to be $\mathcal{O}(10^{-6})$. For the stress, we define the mean relative error associated with the diagonal components of $\boldsymbol{S}_\mathrm{a}$

$$\mathrm{Err}(\boldsymbol{S}_\mathrm{a}) = \max_{J=1,2,3} \left\{ \frac{1}{\mathrm{Vol}(\mathscr{B})} \int_{\mathscr{B}} \frac{(\boldsymbol{S}_\mathrm{a})^{JJ}_{\mathrm{A2}} - (\boldsymbol{S}_\mathrm{a})^{JJ}}{(\boldsymbol{S}_\mathrm{a})^{JJ}_{\mathrm{A2}}} \right\}, \tag{104}$$

where $(\boldsymbol{S}_\mathrm{a})^{JJ}_{\mathrm{A2}}$ is the JJ-component of $\boldsymbol{S}_\mathrm{a}$ evaluated with the aid of the algorithm A2. Also in this case, we obtain $\mathrm{Err}(\boldsymbol{S}_\mathrm{a}) = \mathcal{O}(10^{-6})$. We notice that both $\mathrm{Err}(Z)$ and $\mathrm{Err}(\boldsymbol{S}_\mathrm{a})$ are of the same order of magnitude as the Matlab input RelTol. We remark that, in the simplified model discussed in this section, Z is constant in time and, since material inhomogeneities have been disregarded, it is constant also in space. The stress $\boldsymbol{S}_{\mathrm{a}}$, instead, depends on time through the deformation.

From the estimated errors we can see that the Matlab quadrature method defines a proper approximation of the integrals. Thus, in the following, the results of algorithm A2 can be used as a basis for comparison.

6.2 Inhomogeneous and anisotropic model

In this section, the numerical simulations done with the setting in Table 3 for the simulations with the pseudo-Gaussian distribution, and in Table 6, for the von Mises distribution, are reported and compared one with each other in terms of accuracy and computational time.

First, in order to understand the mechanical response to external stimuli of a biological tissue like articular cartilage, we propose here a Finite Element description of an unconfined compression test (a test that is widely used to estimate the material properties of soft tissues).

In Figure 8, the 2D snapshots of pore pressure, radial filtration velocity, and equivalent von Mises stress are reported in the case of an isotropic tissue without fibres (i.e., with $\phi_{1\mathrm{sR}} = 0$ in (46) and (47)). The required computational effort of such FEM simulation, for which no fibres are considered, consists of a computational time of about 13 seconds, and a memory allocation of about 1.44 Gb. The response of the tissue to the applied incremental compression manifests itself with an increasing pore pressure, which assumes its higher value at the bottom of the sample, whereas the higher velocity is observed at the top external wall of the cylinder. The stress, finally, has its peak at the bottom of the sample, where the tissue is constrained.

As we will see in Figure 12, the addition of fibres as a constituent of the solid phase has the consequence of lowering the maximum value of the pore pressure attained in the domain, and, on the other hand, of increasing the solid stress at the bottom of the sample and the fluid flux at the escaping wall at the top zone of the tissue. The latter behaviour is due to the presence, in that zone, of horizontal fibres. The results of the simulations obtained for an inhomogeneous (both in material properties and probability density distribution) and fibre-reinforced sample of articular cartilage are reported. All the results were obtained from simulations being equipped on an Intel Xeon E5-2620 processor.

In Tables 4 and 5, the computational time and the memory allocation required for the simulations listed in Table 3 and 6 are reported. A comparison of the performances of the FEM simulations in Tables 3 and 6 with the computational effort required by the model with no fibres could give a rough estimate of the time spent by each routine for the only integration.

6.2.1 Results with the pseudo-Gaussian distribution

Table 3 Numerical Tests -pseudo-Gaussian distribution

Name	Integration	N
Sim-1G	SDA, external (A1)	900 equidistributed points
Sim-2G	SDA, internal	200 equidistributed points
Sim-3G	SDA, internal	120 Sloane points
Sim-4G	SDA, internal	21 Sloane points
Sim-5G	SDA, internal	625 equidistributed points
Sim-6G	SDA, internal	41, $(\Theta, \Phi) \in \mathcal{I} \times \mathcal{J}$

In Table 4, the computational time, the memory allocation, and the absolute errors of the SDA simulations, obtained by employing Ψ_1 in the calculations, (both with internal and external implementations) are reported. The absolute errors listed in the table refer to the maximum discrepancies between the values of a given physical quantity, evaluated by using the SDA, and the values of the same quantity obtained by using the algorithm A2. Moreover, the normalised coordinate along the symmetry axis, ξ, for which such absolute discrepancy is maximum is also reported.

Firstly, we notice that both the computational time and the memory allocation are higher if the FEM solver needs to call the external Matlab function. Indeed, we can notice that, in the case of Sim-1G, both the computational time and the memory allocation are higher than in the other five considered cases. In fact, as arguable from the algorithm A1, in the SDA implementation, three nested cycles are required to perform the numerical integration. The first one is on the nodes of the Finite Element mesh, the second and the third are, respectively, on the pairs $(\Theta_i, \Phi_j) \in \mathscr{D}$, with $i = 1, \ldots, m$ and $j = 1, \ldots, n$. However, the simulations Sim-2G—Sim-6G are referred to as *internal*, since the sums over the integration points $(\Theta_i, \Phi_j) \in \mathscr{D}$ are already performed, and an explicit expression of them is provided to the FEM software. On the other hand, the simulation Sim-1G is referred to as *external* because a Matlab code representing the algorithm A1 has been written.

From Figures 9, 10, and 11, obtained by setting $\hat{\Psi} = \hat{\Psi}_1$, we notice that the Sloane sets (Sim-3G and Sim-4G) produce a less accurate result, especially at the top and the bottom zones of the sample, in which

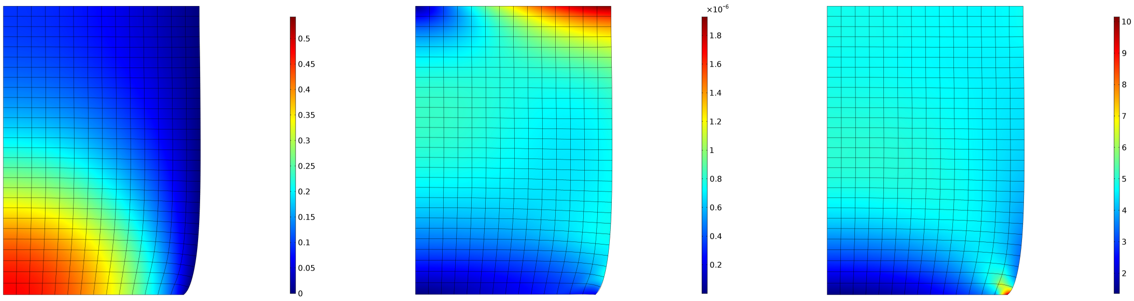

Fig. 8 2D plot of the pore pressure [MPa] (a), norm of the filtration velocity [m/s] (b), and equivalent von Mises stress [MPa] (c) for the model without fibres, respectively.

Table 4 Comparison of the performances, Full model - pseudo-Gaussian distribution

	Sim-1G	Sim-2G	Sim-3G	Sim-4G	Sim-5G	Sim-6G
Comp. Time	9 h 44 min	4 min 45 s	45 s	2 min 42 s	11 min 30 s	15 s
Memory [Gb]	3.75	2.27	2.53	1.97	3.67	1.47
$\lvert Z^{11}_{\mathrm{SDA}} - Z^{11}_{\mathrm{A2}}\rvert$ $(t=0)$	0.0168 $\xi = 0.8884$	0.0502 $\xi = 1$	0.2103 $\xi = 1$	0.1246 $\xi = 1$	0.0202 $\xi = 0.8839$	0.0250 $\xi = 0.1473$
$\lvert Z^{11}_{\mathrm{SDA}} - Z^{11}_{\mathrm{A2}}\rvert$ $(t=20)$	0.0134 $\xi = 0.8661$	0.0398 $\xi = 1$	0.1639 $\xi = 1$	0.1007 $\xi = 1$	0.0161 $\xi = 0.8661$	0.0283 $\xi = 0.1473$
$\lvert Z^{33}_{\mathrm{SDA}} - Z^{33}_{\mathrm{A2}}\rvert$ $(t=0)$	0.0211 $\xi = 0.1473$	0.0318 $\xi = 0.1473$	0.9982 $\xi = 0$	0.0545 $\xi = 0.1205$	0.0253 $\xi = 0.1473$	0.0500 $\xi = 0.1473$
$\lvert Z^{33}_{\mathrm{SDA}} - Z^{33}_{\mathrm{A2}}\rvert$ $(t=20)$	0.0419 $\xi = 0.1384$	0.0618 $\xi = 0.1384$	1.2370 $\xi = 0.0268$	0.1094 $\xi = 0.1250$	0.0419 $\xi = 0.1384$	0.0894 $\xi = 0.1473$
$\lvert(\boldsymbol{S}_{\mathrm{a}})^{11}_{\mathrm{SDA}} - (\boldsymbol{S}_{\mathrm{a}})^{11}_{\mathrm{A2}}\rvert$ [MPa]	0.01106 $\xi = 0.9821$	0.03165 $\xi = 0.9911$	0.14390 $\xi = 1$	0.07200 $\xi = 1$	0.01292 $\xi = 0.9866$	0.00885 $\xi = 0.8527$
$\lvert(\boldsymbol{S}_{\mathrm{a}})^{33}_{\mathrm{SDA}} - (\boldsymbol{S}_{\mathrm{a}})^{33}_{\mathrm{A2}}\rvert$ [MPa]	0.0003870 $\xi = 0.8795$	0.0005079 $\xi = 0.3214$	0.0006323 $\xi = 0.9107$	0.0029116 $\xi = 0.7902$	0.0004852 $\xi = 0.8750$	0.0040588 $\xi = 0.9196$

fibres are horizontally and vertically aligned, respectively. This is possibly due to the fact that, to apply the SDA with such sets of points, we need to select a subset of each spherical design proposed by Sloane to restrict the integration to $\mathbb{S}^{2+}_X\mathscr{B}$ rather than to $\mathbb{S}^2_X\mathscr{B}$. Moreover, in contrast to what has been done in Section 4.2, where the integration with respect to Φ was exact, here the SDA implementation inside the FE discretisation solves numerically also the integration with respect to Φ. Thus, the lack in accuracy of Sim-3G and Sim-4G, which can be registered in Figures 9, 10, and 11, is influenced by the choice of the longitudes Φ_j in the pairs $(\Theta_i, \Phi_j) \in \mathscr{D}$, with $i = 1, \dots, m$ and $j = 1, \dots, n$.

In Sim-1G, Sim-2G and Sim-5G, which refer to sets of equidistributed points, it can be noticed that the computed discrepancy between Matlab and the SDA outcomes decreases, as expected, while increasing the number of points in $\mathscr{D}$. Sim-1G, in particular, has the highest number of points in the spherical design, obtained with $m = n = 30$, and returns the smallest errors (see Table 4) for all the required integrals. Unfortunately, the computational effort that such simulation requires is three times higher than the one performed with the Matlab routine. Indeed, concerning the computational time and the memory allocation required by the Matlab integration coupled with the FEM, we registered, on the same workstation and with the same numerical setting, an elapsed time of about 3 h and 40 min, with a memory allocation of about 2.6 Gb. Also in this case, this was due to the external Matlab call. To obtain the curves in Sim-2G and Sim-5G, respectively, we set $m = 20$ and $m = 25$.

Finally, the simulation performed with the set proposed in this manuscript, $\mathcal{I} \times \mathcal{J}$ (Sim-6G), can be expressed as

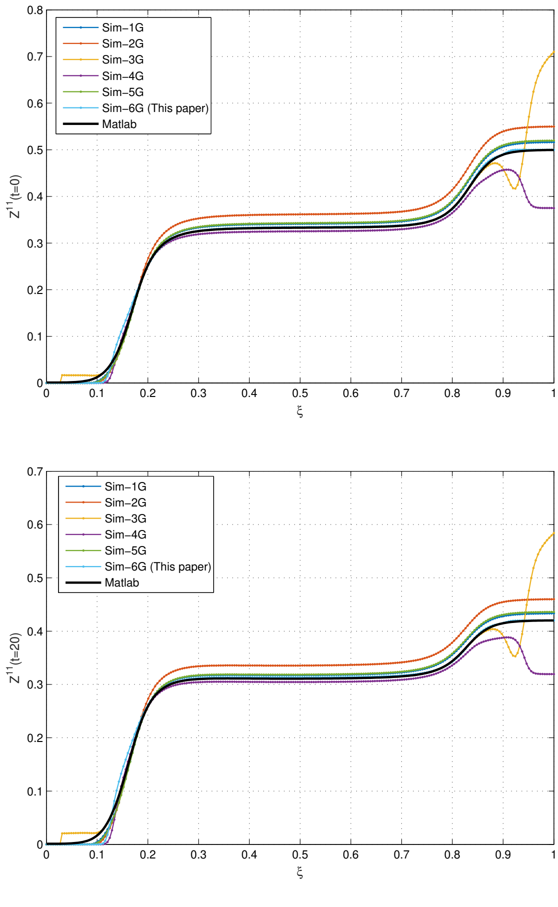

Fig. 9 Radial component Z^{11} of the averaged structure tensor $\boldsymbol{Z}$ vs the normalised depth. (a) Evaluation at $t = 0$ s (see also [22] for comparison). (b) Evaluation at $t = 20$ s. The probability density is the pseudo-Gaussian distribution in both cases.

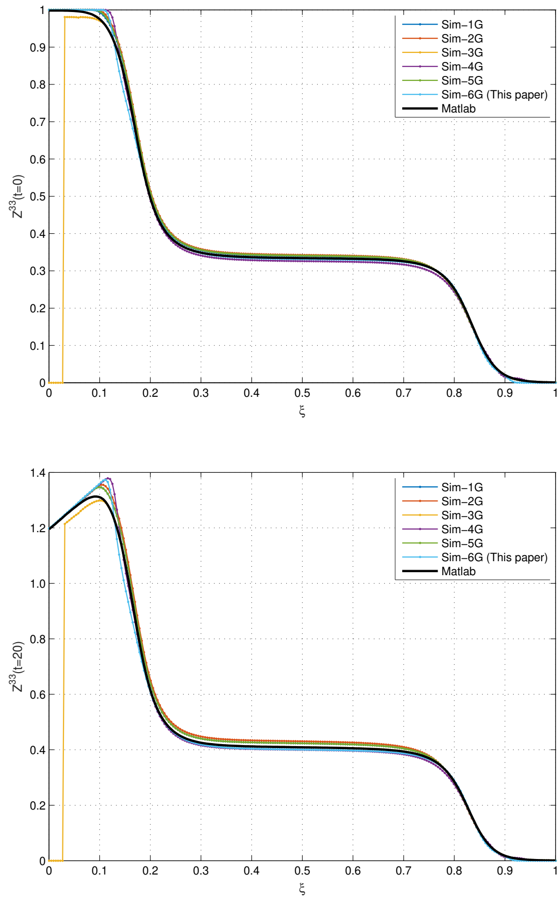

Fig. 10 Axial component Z^{33} of $\boldsymbol{Z}$ vs the normalised depth. (a) Evaluation at $t = 0$ s (see also [22] for comparison). (b) Evaluation at $t = 20$ s. The probability density is the pseudo-Gaussian distribution in both cases.

$$\int_{\mathbb{S}^2_+ \mathscr{B}} f(\boldsymbol{M}) \simeq \frac{2\pi}{N} \left(\sum_{i=2}^{6} \sum_{j=1}^{8} f(\mathcal{X}_{ij}) + f(0, \Phi) \right). \tag{105}$$

We can notice from Table 4 that $\mathcal{I} \times \mathcal{J}$ produces errors in capturing the radial and axial components of $\boldsymbol{Z}$ that are comparable with the ones obtained with Sim-1G and Sim-5G, and even a better estimate of $(\boldsymbol{S}_{\mathrm{a}})^{11}$. Moreover, since $\mathcal{I} \times \mathcal{J}$ contains a smaller number of pairs $\mathcal{X}_{ij}$, its implementation produces the fastest results. Indeed, even if an internal implementation of the points employed in Sim-1G is performed, its computational effort would be greater than, or equal to, the one registered for Sim-5G. Thus, the set $\mathcal{I} \times \mathcal{J}$ gives us, for the considered set of numerical tests in Table 3, results that are comparable with those of Sim-1G, but with a faster and lighter implementation. A less acceptable result, however, is obtained for $(\boldsymbol{S}_{\mathrm{a}})^{33}$ (see Figure 11b), for which the computed error is one order of magnitude bigger than the one obtained for Sim-1G. In particular, for that component of the tensor $\boldsymbol{S}_{\mathrm{a}}$, the smaller error is obtained with the set $\mathcal{S}'_{120}$. Such set of points, as visible from Figures 13, 14, and 15, is the one that, coherently with the preliminary analysis done in Section 4.2, returns the better result if $\hat{\Psi}_2$ is employed.

As a consequence of a different outcome of the SDA, depending on the choice of the spherical design, the characteristic values of pore pressure, fluid filtration velocity and stress of the whole solid could change more or less remarkably. In analysing the mechanical response of articular cartilage, it is important to have a good estimate of the pressure and the stresses that accumulate in the tissue undergoing a finite deformation. In the following, the consequences of the addition of the fibres in the model, and the consequences that a less accurate SDA could yield, are discussed.

In Figure 12 the time evolution of the pore pressure, the filtration velocity (radial component) and the von Mises equivalent stress have been reported, respectively,

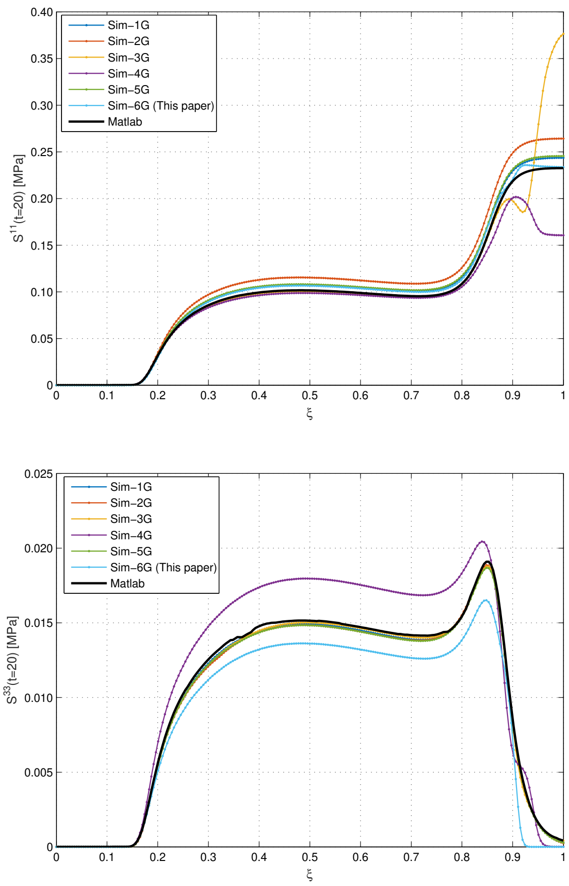

Fig. 11 Radial (a) and axial (b) components of $\boldsymbol{S}_{\mathrm{a}}$ vs the normalised depth. Evaluation at $t = 20$ s. Pseudo-Gaussian distribution.

from left to right. All these quantities are evaluated in those points of the domain in which they attain the maximum value. Thus, as visible also from Figures 8, for the pressure we take the origin of the coordinate system, for the filtration velocity we take the upper external point, and for the solid stress the maximum value is at the bottom external point, where the sample is fixed.

As we can see from Figure 12, the pressure (Figure 12a) obtained without adding the fibres in the model is greater than the one obtained by considering them. Conversely, the filtration velocity (Figure 12b) is increased by the presence of horizontally aligned fibres. This is due to the fact that, in the top zone of the domain, the fibres facilitate the radial flow going outward the sample. Finally, the equivalent von Mises stress (Figure 12c) is amplified by the presence of the fibres. The artifacts arising due to unsatisfactory results of the SDA are visible particularly in Figure 12b. Indeed, since in the upper part of the domain the Sloane sets of points do not capture in a proper way the values of Z^{11}, we see that the profile of the filtration velocity obtained as an outcome of Sim-3G and Sim-4G shows a strong discrepancy with respect to the other employed spherical designs and the Matlab outcomes. The inaccuracy of the SDA is less evident in the plots of the pore pressure and the solid stress (Figure 12a and 12c, respectively), possibly because the order of magnitude of such quantities (MPa), evaluated in their maximum points, are greater than the ones registered for the related errors, as shown in Tables 4 and 5 for the solid stress. Finally, the pale blue, marked curve, which corresponds to Sim-6G, is almost overlapped to the black one, representing the Matlab outcome in all the three plots in Figure 12.

6.2.2 Results with the von Mises distribution

The performed simulations with the von Mises distribution aim principally to verify the goodness of the set $\mathcal{S}'_{120}$, and to compare the results obtained by employing it with the ones obtained with the entire set $\mathcal{S}_{240}$, i.e., with the integration over $\mathbb{S}^2_X\mathscr{B}$. Indeed, differently from the pseudo-Gaussian distribution, it holds that $\hat{\Psi}_2(\xi,\Theta) = \hat{\Psi}_2(\xi,\Theta+\pi)$. Thus, first we aim to compare the solutions obtained with 240 and 120 Sloane points in Sim-2VM and Sim-3VM, respectively. A set of equidistributed points is considered in Sim-1VM, together with the set $\mathcal{S}'_{21}$ (Sim-4VM) and our set $\mathcal{I}\times\mathcal{J}$ (Sim-5VM). In Table 5, the computational time, allocated memory, and the absolute errors in computing the values of Z^{11}, Z^{33}, $(\boldsymbol{S}_{\mathrm{a}})^{11}$ and $(\boldsymbol{S}_{\mathrm{a}})^{33}$ are reported.

Due to the symmetry properties of $\hat{\Psi}_2$, the performances of Sim-2VM and Sim-3VM are perfectly equivalent. Indeed, as visible from Figures 13, 14, and 15, their results overlap completely.

Again, as visible from Figures 13, 14, and 15a, the set of points proposed in the present work performs well in capturing $\boldsymbol{Z}$ and the radial component of the stress. Indeed, for such curves, the outcomes of the spherical design $\mathcal{I}\times\mathcal{J}$ almost overlap, or are relatively less distant from the outcomes of the Matlab routine and the SDA with $\mathcal{S}'_{120}$, or $\mathcal{S}_{240}$, equivalently. However, the set of points is not properly capturing, also in the case of the von Mises distribution, the axial component of $\boldsymbol{S}_{\mathrm{a}}$. The less accurate results are, instead, obtained by means of the 500 equidistributed points, which show the same degree of accuracy as the set $\mathcal{S}'_{21}$, but require a greater computational effort.

We omit the graphs related to the pore pressure, velocity and stress in the present case, since the amount of error registered for the numerical tests here discussed, i.e., the ones in Table 6, are not sufficiently big, as in

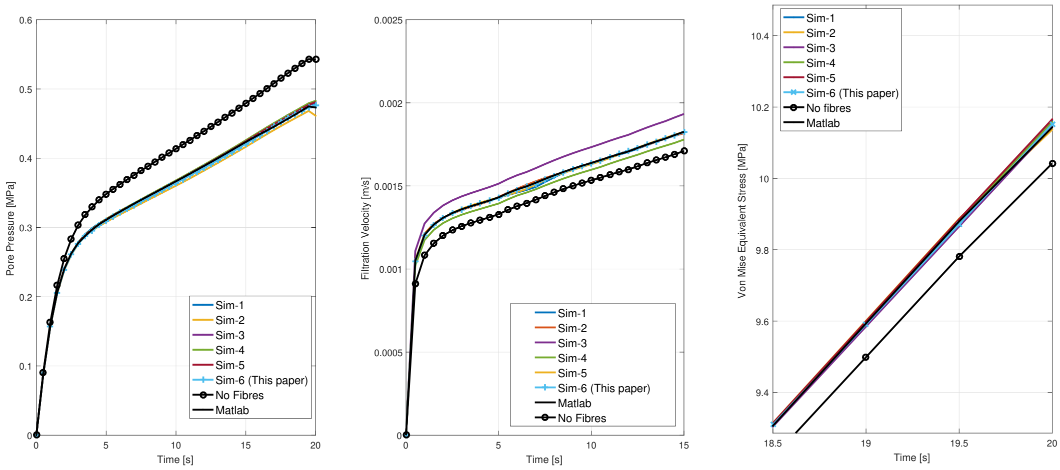

Fig. 12 (a) Pointwise evaluation (in the point $P = (0, 0, 0)$ mm) of the pore pressure over the time. (b) point-wise evaluation (in the point $P = (0.5, 0.5, 1)$ mm of the filtration velocity over the time. (c) Pointwise evaluation (in the point $P = (0.5, 0.5, 0)$ mm) of the equivalent von Mises stress over the time. A zoom of the same curve is reported, due to the strong vicinity of each curve in the graph.

Table 5 Comparison of the performances, Full model - von Mises distribution

	Sim-1VM	Sim-2VM	Sim-3VM	Sim-4VM	Sim-5VM
Comp. Time	13 min 39 s	3 min 11 s	2 min 42 s	42 s	16 s
Memory [Gb]	3.45	2.71	2.06	1.66	1.61
$\lvert Z^{11}_{\mathrm{SDA}} - Z^{11}_{\mathrm{A2}}\rvert$ $(t = 0)$	0.0489 $\xi = 0.9464$	0.0046 $\xi = 0.4062$	0.0046 $\xi = 0.4062$	0.0487 $\xi = 1.0000$	0.0217 $\xi = 0.3125$
$\lvert Z^{11}_{\mathrm{SDA}} - Z^{11}_{\mathrm{A2}}\rvert$ $(t = 20)$	0.0401 $\xi = 0.7500$	0.0034 $\xi = 0$	0.0034 $\xi = 0$	0.0401 $\xi = 0.9911$	0.0220 $\xi = 0.3214$
$\lvert Z^{33}_{\mathrm{SDA}} - Z^{33}_{\mathrm{A2}}\rvert$ $(t = 0)$	0.0455 $\xi = 0.3929$	0.0092 $\xi = 0.4062$	0.0092 $\xi = 0.4062$	0.0625 $\xi = 0.0223$	0.0433 $\xi = 0.3125$
$\lvert Z^{33}_{\mathrm{SDA}} - Z^{33}_{\mathrm{A2}}\rvert$ $(t = 20)$	0.1050 $\xi = 0.2143$	0.0233 $\xi = 0.1786$	0.0233 $\xi = 0.1786$	0.1339 $\xi = 0.1786$	0.0732 $\xi = 0.0.3304$
$\lvert(\boldsymbol{S}_{\mathrm{a}})^{11}_{\mathrm{SDA}} - (\boldsymbol{S}_{\mathrm{a}})^{11}_{\mathrm{A2}}\rvert$ [MPa]	0.0289 $\xi = 0.9821$	0.0051 $\xi = 0.5357$	0.0051 $\xi = 0.5357$	0.0265 $\xi = 0.8973$	0.0138 $\xi = 0.5670$
$\lvert(\boldsymbol{S}_{\mathrm{a}})^{33}_{\mathrm{SDA}} - (\boldsymbol{S}_{\mathrm{a}})^{33}_{\mathrm{A2}}\rvert$ [MPa]	0.0013 $\xi = 0.5446$	0.0009 $\xi = 0.5179$	0.0009 $\xi = 0.5179$	0.0038 $\xi = 0.5045$	0.0043 $\xi = 0.8170$

Table 6 Numerical Tests - von Mises distribution

Name	Integration	N
Sim-1VM	SDA, internal	500 equidistributed points
Sim-2VM	SDA, internal	240 Sloane points
Sim-3VM	SDA, internal	120 Sloane points
Sim-4VM	SDA, internal	21 Sloane points
Sim-5VM	SDA, internal	41, $(\Theta, \Phi) \in \mathcal{I} \times \mathcal{J}$

the previous case, to produce strong discrepancies in such physical quantities of the model.

7 Conclusions and future work

In this work, we analysed the performances of a numerical procedure, the SDA, which is often employed to compute the permeability and the mechanical stresses in highly anisotropic, fibre-reinforced, composite materials. In particular, we addressed composite materials of

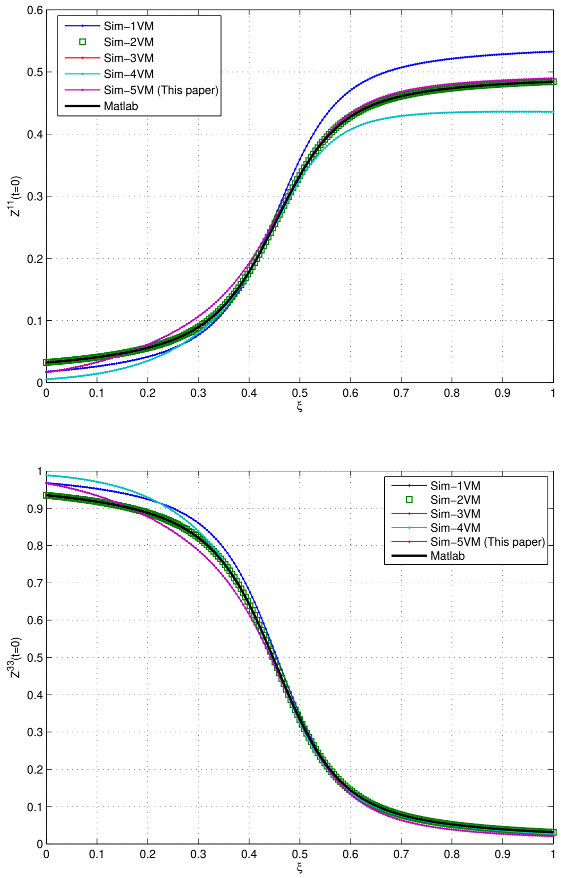

Fig. 13 (**a**) Radial component Z^{11} and (**b**) axial component Z^{33} of $\boldsymbol{Z}$ versus the normalised depth at time $t = 0\,\mathrm{s}$. For these simulations, the probability density is the von Mises distribution.

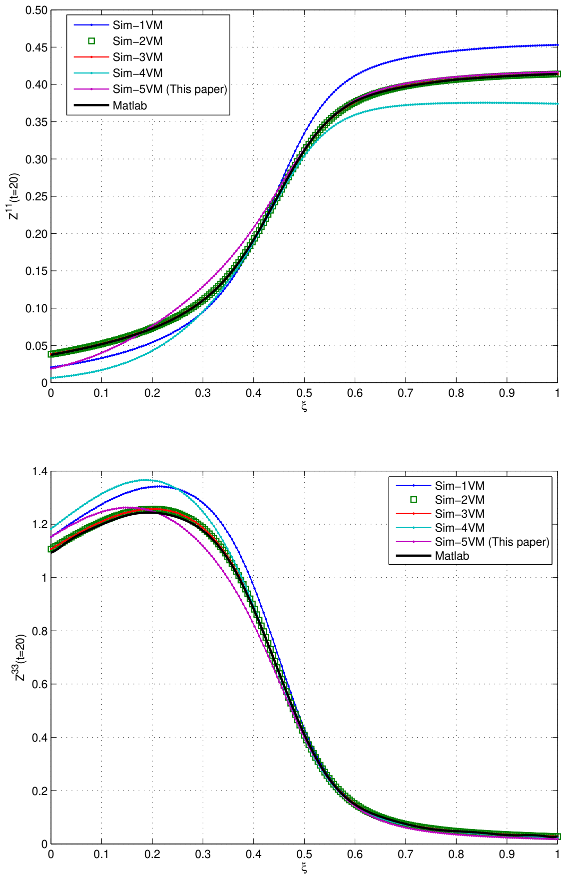

Fig. 14 (**a**) Radial component Z^{11} and (**b**) axial component Z^{33} of $\boldsymbol{Z}$ versus the normalised depth at time $t = 20\,\mathrm{s}$. For these simulations, the probability density is the von Mises distribution.

biomechanical interest, in which the fibre-reinforcement is due to the presence of collagen fibres, as is the case for articular cartilage. The mathematical model, within which the SDA has been implemented, has been taken from [58], and leads to a set of coupled and highly nonlinear partial differential equations, whose weak form is written in (51a) and (51b) [31]. These equations have to be solved in conjunction with the constitutive expressions defining the mechanical stress and the permeability of the tissue. The core issue of the problem is given, in fact, by the integrals associated with the anisotropic parts of these two properties of the tissue (cf. (46) and (47)), in which the coupling between the directionality of the material response, expressed by the structure tensor $\boldsymbol{A}$, and its evolution with the deformation are accounted for by the invariant $I_4 = \mathrm{tr}(\boldsymbol{C}\boldsymbol{A})$. In the majority of the cases, these integrals cannot be evaluated analytically. More importantly, due to the coupling between $\boldsymbol{A}$ and $\boldsymbol{C}$, they cannot be even solved numerically once for all, since they have to be updated at each step of the deformation evolution. This calls for the implementation in a FEM code of dedicated quadrature schemes, such as the SDA, on the fly.

With the motivation outlined above, we underlined some problematic issues of the SDA, such as the strong dependence on the choice of both the number and the placement of the quadrature nodes that this scheme requires. After a first analysis on the performance of the SDA against a comparative quadrature method, the SDA (see algorithm A1) has been implemented in a way to be coupled with a commercial FEM software. This has been done with the aim of testing the software through the simulation of a well-established benchmark problem, employed for studying the hydraulic and mechanical properties of hydrated soft tissues: namely, the unconfined compression test in displacement control of a cartilage sample. The results of the FE simulations have been performed with the goal of comparing reciprocally different point sets adopted for the SDA. Their reliability has been tested by comparison with

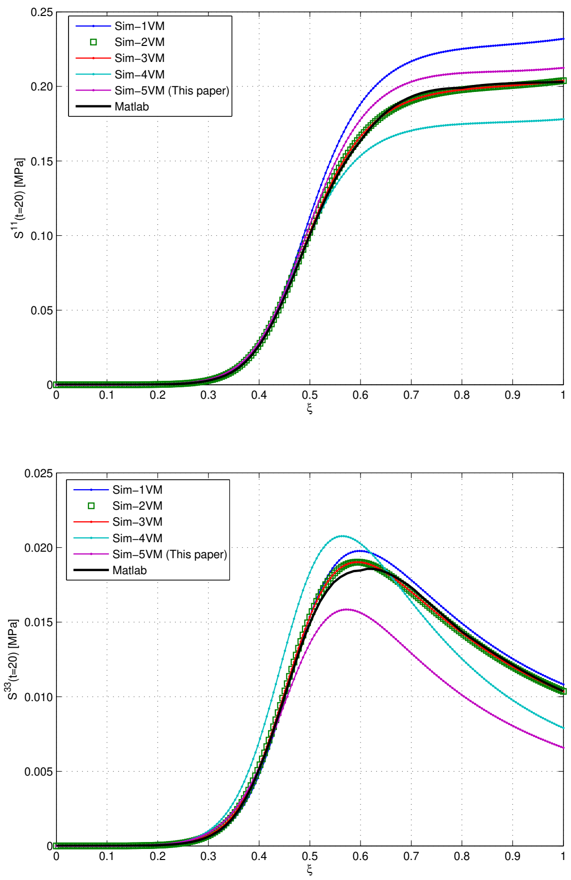

Fig. 15 Radial (a) and axial (b) components of $\boldsymbol{S}_{\mathrm{a}}$ vs the normalised depth. Evaluation at $t = 20$ s. The probability density is the von Mises distribution.

the quadrature scheme A2, available in Matlab. After such analysis, we designed a set of points, i.e., the one represented in (65a) and (65b), which, in this work, gave us the best feedback in computing the anisotropic part of permeability and mechanical stress.

From the analysis of the performances reported in Tables 4 and 5, we deduce that, if the quadrature points are properly chosen, an internal implementation of the SDA is in general preferable to an external Matlab call. However, the latter is faster and more accurate than the SDA, if the points on the hemisphere are chosen in a way to be equidistributed. We discuss here the performances of the set of points $\mathcal{I} \times \mathcal{J}$ for which, as visible throughout the present work, we obtain a small computational effort, with acceptable results in capturing the main quantities of interest for the problem at hand. The set of points $\mathcal{I} \times \mathcal{J}$ is easy to implement by writing a relatively small list of summands, and by performing the sums required in the SDA routine without a recursive and nested procedure. This is due to the fact that $\mathcal{I} \times \mathcal{J}$ has only 41 points, which in turn are conceived for the integration over the hemisphere, thereby addressing the material and geometrical symmetries of the considered problem. As discussed in Section 6, the performances of such set are, in most of the cases, comparable to those returning acceptable, even if heavier, results.

To validate the set $\mathcal{I} \times \mathcal{J}$ for a more general computational and mathematical setting, we need to test it on a wider range of benchmark problems and constitutive laws. Moreover, we remark that there might be cases in which the choice of the point set, which is necessary to achieve the best approximation of a given physical quantity, has to be done adaptively. These tasks shall be the subject of our future investigations on this theme. For the sake of completeness, we finally notice that the reduced 2D model studied in this work (justified by the geometric and material symmetries of the considered medium) should be extended to realistic three-dimensional geometries. This is important also in view of generalising the presented framework to biomechanical problems in which the fluid flow may deviate from the Darcian regime or growth and remodelling occur.

References

1. Ascher, U. M., Petzold, L. R.: *Computer Methods for Ordinary Differential Equations and Differential-Algebraic Equations*, SIAM, Philadelphia, 1998, ISBN 0-89871-412-5.
2. Aspden, R.M., Hukins, D.W.L.: Collagen organization in articular cartilage, determined by X-ray diffraction, and its relationship to tissue function, *Proc. R. Soc. B*, 212:299–304, 1981.
3. Ateshian, G.A.: On the theory of reactive mixtures for modeling biological growth. *Biomech. Model. Mechanobiolg.*, 6:423–445, 2007
4. Ateshian, G.A., Weiss, J.A., Anisotropic Hydraulic Permeability Under Finite Deformation. *J. Biomech. Eng.*, 132 :111004-1–111004-7, 2010.
5. Baaijens, F., Bouten, C., Driessen, N.: Modeling collagen remodeling, *Journal of Biomechanics*, 43:166–175, 2010.
6. Bažant, P., Oh, B.H.: Efficient numerical integration on the surface of a hemisphere, *ZAMM–Zeitschrift für Angewandte Mathematik und Mechanik/Journal of Applied Mathematics and Mechanics*, 66(1):37–49, 1986.
7. Bear, J, Bachmat, Y., *Introduction to modeling of transport phenomena in Porous Media*, Kluwer, Dordrecht, Boston, London, 1990.
8. Beentjes C.H.L., Quadrature on a spherical surface. Technical Report, University of Oxford (2015).
9. Bennethum, L.S., Murad, M.A., Cushman, J.H.: Macroscale thermodynamics and the chemical potential for swelling porous media, *Transp. Porous Media*, 39:187–225, 2000.
10. Bennethum, L.S., Giorgi, T., Generalized Forchheimer equation for two-phase flow based on hybrid mixture theory, *Transp. Porous Media*, 26 (1997), pp. 261–275.
11. Bonet, J., Wood, R.D.: *Nonlinear Continuum Mechanics for Finite Element Analysis*, Cambridge University Press, 1997.

12. Brauchart, J.S., Grabner, P.: Distributing many points on the spheres: Minimal energy and designs, *J. Complexity*, 31:293–326, 2015
13. Byrne, H.M., Preziosi, L.: Modelling solid tumour growth using the theory of mixtures, *Math. Med. Biol.*, 20:341–366, 2004.
14. Delsarte, P., Goethals, J.M., Seidel, J.J.: Spherical codes and designs, *Geometriae Dedicata*, 6:363–388, 1977.
15. Federico, S., Grillo, A.: Linear Elastic Composites with Statistically Oriented Spheroidal Inclusions. In: Meguid, S.A., Weng, S.J. (eds) A Book Chapter in Advances in Micromechanics and Nanomechanics of Composite Solids. Springer (2017).
16. Federico, S.: Porous materials with statistically oriented reinforcing fibres. In L. Dorfmann and R.W. Ogden, editors, *Nonlinear Mechanics of Soft Fibrous Materials*, 49–120, Springer, Berlin, Germany, 2015. CISM Courses and Lectures No. 559, International Centre for Mechanical Sciences.
17. Federico, S., Grillo, A., La Rosa, G., Giaquinta, G., Herzog, W.: A transversely isotropic, transversely homogeneous microstructural-statistical model of articular cartilage, *Journal of Biomechanics*, 38:2008–2018, 2005.
18. Federico, S., Gasser, T.C.: Nonlinear elasticity of biological tissues with statistical fibre orientation, *J. R. Soc. Interface*, 7:955–966, 2010.
19. Federico, S., Grillo, A., Elasticity and permeability of porous fibre-reinforced materials under large deformations, *Mech. Mat.*, 44 (2012), pp. 58–71.
20. Federico, S., Herzog, W.: On the anisotropy and inhomogeneity of permeability in articular cartilage, *Biomech. Model. Mechanobiol.*, 7:367–378, 2008.
21. Federico, S., Herzog, W.: Towards an analytical model of soft biological tissues, *J. Biomech.*, 41:3309–3313, 2008.
22. Federico, S., Herzog, W.: On the permeability of fibre-reinforced porous materials, *Int. J. Solids Struct.*, 45:2160–2172, 2008.
23. Garikipati, K., Arruda, E.M., Grosh, K., Narayanan, H., Calve, S.: A continuum treatment of growth in biological tissue: the coupling of mass transport and mechanics, *Journal of the Mechanics and Physics of Solids*, 52:1595–1625, 2004.
24. Gasser, T.C., Ogden, R.W., Holzapfel, G.A.: Hyperelastic modelling of arterial layers with distributed collagen fibre orientations. *J Roy Soc Interface*, 3:15–35, 2006.
25. Grillo, A., Zingali, G., Borrello, D., Federico, S., Herzog, W., Giaquinta, G.: A multiscale description of growth and transport in biological tissues, *Theoret. Appl. Mech.*, 34(1):51–87, 2007.
26. Grillo, A., Federico, S., Wittum, G.: Growth, mass transfer, and remodeling in fiber-reinforced, multi-constituent materials, *International Journal of Non-Linear Mechanics*, 47:388–401, 2012.
27. Grillo, A., Giverso, C., Favino, M., Krause, R., Lampe, M., Wittum, G., "Mass Transport in Porous Media with Variable Mass". In *Numerical Analysis of Heat and Mass Transfer in Porous Media—Advanced and Structural Materials*, J.M.P.Q. Delgado, A.G.B. de Lima, and M.V. da Silva, eds., Springer-Verlag, Berlin, Heidelberg, pp. 27–61.
28. Grillo, A., Carfagna, C., Federico, S.: The Darcy-Forchheimer law for modelling fluid flow in biological tissues, *Theort. Appl. Mech. TEOPM7*, 41(4):283–322, 2014.
29. Grillo, A., Guaily, A., Giverso, C., Federico, S.: Non-Linear Model for Compression Tests on Articular Cartilage, *Journal of Biomechanical Engineering*, 137:071004-1–071004-8, 2015.
30. Grillo, A., Wittum, G., Tomic, A., Federico, S., Remodelling in statistically oriented fibre-reinforced materials and biological tissues, *Mathematics and Mechanics of Solids*, 20(9):1107–1129, 2015.
31. Grillo, A., Prohl, R., Wittum, G.: A poroplastic model of structural reorganisation in porous media of biomechanical interest, *Continuum Mechanics and Thermodynamics*, 28:579–601, 2016.
32. Guilak, F., Ratcliffe, A., Mow, V.C.: Chondrocyte deformation and local tissue straining articular cartilage: a confocal microscopy study, *J. Orthopaedic Res.*, 13:410–421, 1995.
33. Hardin, R.H., Sloane, N.J.A.: McLaren's Improved Snub Cube and Other New Spherical Designs in Three Dimensions, *Discrete and Computational Geometry*, 15:429–441, 1996.
34. Hashlamoun, K., Grillo, A., Federico, S.: Efficient evaluation of the material response of tissues reinforced by statistically oriented fibres, *Z. Angew. Math. Phys.*, 2016, 67:113, 2016 DOI 10.1007/s00033-016-0704-5.
35. Hassanizadeh, M.S.: Derivation of basic equations of mass transport in porous media. Part II. Generalized Darcy's and Fick's Laws, *Adv. Water Resour.*, 9:208–222, 1986.
36. Holmes, M.H., Mow, V.C.: The nonlinear characteristics of soft gels and hydrated connective tissues in ultrafiltration, *J. Biomech.*, 23:1145–1156, 1990.
37. Holzapfel, G.A., Gasser, T.C., Ogden, R.W.: A new constitutive framework for arterial layers with distributed collagen fibre orientations, *Journal of Elasticity*, 61:1–48, 2000.
38. http://neilSloane.com/sphdesigns/dim3/
39. Huyghe, J.M., Van Loon, R., Baaijens, F.T.P.: Fluid-solid mixtures and electrochemomechanics: the simplicity of Lagrangian mixture theory, *Computational and Applied Mathematics*, 23(2-3):235–258, 2004.
40. Iserles, A.: *A First Course in the Numerical Analysis of Differential Equations*, Cambridge University Press, 1996, ISBN 978-0-521-55655-2.
41. Klisch, S.M., Chen, S.S., Sah, R.L., Hoger, A.: A growth mixture theory for cartilage with application to growth-related experiments on cartilage explants, *Journal of Biomechanical Engineering*, 125:169–179, 2003.
42. Landau, L.D., Lifshitz, E.M.: *Electrodynamics of Continuous Media*, Pergamon Press, Oxford, 1960.
43. Lanir, Y.: Constitutive equations for fibrous connective tissues, *J. Biomech.*, 16:1–12, 1983.
44. Lebedev, V.I.: Quadratures on a sphere. *USSR Computational Mathematics and Mathematical Physics*, 16(2):10–24, 1976.
45. Loret, B., Simões, F.M.F.: A framework for deformation, generalized diffusion, mass transfer and growth in multi-species multi-phase biological tissues, *European Journal of Mechanics A/Solids*, 24:757–781, 2005.
46. Mansour, J.M.: *Biomechanics of cartilage*, Chapter 5, pp.66–67. In *Kinesiology: the mechanics and pathomechanics of human movement*, Oatis, C.A. (Ed.), Lippincott Williams & Wilkins, Philadelphia, 2003.
47. Marsden, J.E., Hughes, T.J.R.: *Mathematical Foundations of Elasticity.* Dover Publications Inc., New York, 1983
48. McLaughlin, R.: A study of the differential scheme for the composite materials, *Int. J. Eng. Sci.*, 15:237–244, 1977.
49. Menzel, A.: Modelling of anisotropic growth in biological tissues, *Biomech Model Mechanobiol*, 3:147–171, 2005.
50. Mollenhauer, J., Aurich, M., Muehleman, C., Khelashvilli, G., Irving, T.C.: X-ray diffraction of the molecular substructure of human articular cartilage, *Connective Tissue Res.*, 44:201–207, 2003.

51. Norris, A.N.: A differential scheme for the effective moduli of composites, *Mech. Mater.*, 4:1–16, 1985.
52. Pezzuto, S., Ambrosi, D.: Active contraction of the cardiac ventricle and distortion of the microstructural architecture, *Int J Numer Meth Biomed Eng*, 30(12):1578–1596, 2014.
53. Podzniakov, S., Tsang, C.F.: A self-consistent approach for calculating the effective hydraulic conductivity of a binary, heterogeneous medium, *Warter Resour. Res.*, 40:1–13, 2004.
54. Quiligotti, S.: On bulk growth mechanics of solid-fluid mixtures: kinematics and invariance requirements, *Theoret. Appl. Mech.*, 28:1–11, 2002.
55. Quiligotti, S., Maugin, G.A., dell'Isola, F.: An Eshelbian approach to the nonlinear mechanics of constrained solid-fluid mixtures, *Acta Mech.*, 160:45–60, 2003.
56. Römgens, A.M., van Donkelaar, C.C., Ito, K.: Contribution of collagen fibres to the compressive stiffness of cartilaginous tissues. *Biomech Model Mechanobiol*, 12(6):1221–1231, 2013.
57. Skacel, P., Bursa, J.: Numerical implementation of constitutive model for arterial layers with distributed collagen fibre orientations, *Computer Methods in Biomechanics and Biomedical Engineering*, 18(8): 816–828, 2015.
58. Tomic, A., Grillo, A., Federico, S.: Poroelastic materials reinforced by statistically oriented fibres—numerical implementation and application to articular cartilage, *IMA Journal of Applied Mathematics*, 79:1027–1059, 2014.
59. Weisstein, E.W.: *Sphere Point Picking.* From MathWorld–A Wolfram Web Resource. http://mathworld.wolfram.com/SpherePointPicking.html
60. Wilson, W., Driesseny, N.J.B., van Donkelaar, C.C., Ito K.: Prediction of collagen orientation in articular cartilage by a collagen remodeling algorithm, *Osteoarthritis and Cartilage*, 14:1196–1202, 2006.